

Non-proportional loading in sequentially linear analysis for 3D stress states

Pari, Manimaran; Hendriks, Max A.N.; Rots, Jan G.

DOI

[10.1002/nme.6060](https://doi.org/10.1002/nme.6060)

Publication date

2019

Document Version

Final published version

Published in

International Journal for Numerical Methods in Engineering

Citation (APA)

Pari, M., Hendriks, M. A. N., & Rots, J. G. (2019). Non-proportional loading in sequentially linear analysis for 3D stress states. *International Journal for Numerical Methods in Engineering*, 119(6), 506-531.
<https://doi.org/10.1002/nme.6060>

Important note

To cite this publication, please use the final published version (if applicable).
Please check the document version above.

Copyright

Other than for strictly personal use, it is not permitted to download, forward or distribute the text or part of it, without the consent of the author(s) and/or copyright holder(s), unless the work is under an open content license such as Creative Commons.

Takedown policy

Please contact us and provide details if you believe this document breaches copyrights.
We will remove access to the work immediately and investigate your claim.

Green Open Access added to TU Delft Institutional Repository

'You share, we take care!' - Taverne project

<https://www.openaccess.nl/en/you-share-we-take-care>

Otherwise as indicated in the copyright section: the publisher is the copyright holder of this work and the author uses the Dutch legislation to make this work public.

RESEARCH ARTICLE

WILEY

Non-proportional loading in sequentially linear analysis for 3D stress states

Manimaran Pari¹  | Max A.N. Hendriks^{1,2} | Jan G. Rots¹

¹Faculty of Civil Engineering and Geosciences, Delft University of Technology, Delft, The Netherlands

²Department of Structural Engineering, Norwegian University of Science and Technology (NTNU), Trondheim, Norway

Correspondence

Manimaran Pari, Faculty of Civil Engineering and Geosciences, Delft University of Technology, 2628 GA Delft, The Netherlands.
Email: m.pari@tudelft.nl

Funding information

Nederlandse Aardolie Maatschappij B.V. (NAM), Grant/Award Number: UI46268

Summary

Sequentially linear analysis (SLA), a non-incremental-iterative approach towards finite element simulation of quasi-brittle materials, is based on sequentially identifying a critical integration point in the model, to reduce its strength and stiffness, and the associated critical load multiplier (λ_{crit}), to scale the linear analysis results. In this article, two novel methods are presented to enable SLA simulations for non-proportional loading situations in a three-dimensional fixed smeared crack framework. In the first approach, the cubic function in the load multiplier is analytically solved for real roots using trigonometric solutions or the Cardano method. In the second approach, the load multiplier is expressed as a function of the inclination of a potential damage plane and is deduced using a constrained optimization approach. The first method is preferred over the second for the validation studies due to computational efficiency and accuracy reasons. A three-point bending beam test, with and without prestress, and an RC slab tested in shear, with and without axial loads, are used as benchmarks. The proposed solution method shows good agreement with the experiments in terms of force-displacement curves and damage evolution.

KEYWORDS

fixed smeared crack model, non-proportional loading, quasi-brittle materials, sequentially linear analysis (SLA), 3D stress states

1 | INTRODUCTION

Nonlinear finite element analyses (NLFEA) of civil engineering structures/specimen made of quasi-brittle materials, characterized by strain softening, have always had the so-called *convergence troubles*. The incremental-iterative nature of the solution procedure pushes multiple integration points into softening simultaneously and this can affect the positive definite nature of the global stiffness matrix, resulting in the ill-conditioning of the finite element formulation. Several path-following techniques like the arc-length control, crack mouth opening displacement control, and energy release control¹ address this problem but are sophisticated techniques, thus requiring user expertise in NLFEA. The use of tangent stiffness was identified to be one of the potential causes and several secant stiffness-based approaches were devised, one of which is the sequentially linear analysis (SLA) technique and is non-incremental (total) in nature.²⁻⁴ The choice of a total approach in combination with the use of discretized constitutive relations, called the *saw-tooth laws* with successively reducing secant stiffnesses and strengths, helped circumvent the aforementioned problems. The procedure begins with finding a unique integration point where the current strength has been violated (that corresponds to the one with the

minimum of all load multipliers from the integration points in the model), followed by scaling the linear analysis results with the corresponding load multiplier and imparting damage to the critical point by reducing its stiffness and strength based on the saw-tooth laws, and eventually returns to a new linear analysis on the damaged model. The definition of the load multiplier for each integration point i and the resulting critical load multiplier per analysis step j are shown in the following in a general sense, where $f_i^{(j)}$ and $\sigma_{\text{gov};i}$ are the current allowable strength based on the saw-tooth law and the governing stress, respectively:

$$\lambda_i^{(j)} = \frac{f_i^{(j)}}{\sigma_{\text{gov};i}^{(j)}}, \quad \lambda_{\text{crit}}^{(j)} = \min_i \left(\lambda_{\text{crit};i}^{(j)} \right) \quad \text{for all } \lambda_{\text{crit};i}^{(j)} > 0. \quad (1)$$

SLA is thus an event-by-event approach, ie, one linear analysis is performed at a time to identify a critical integration point and the method thereby avoids the problem associated with the regular incremental-iterative procedures with respect to convergence as it traces through every event, ie, a jump or snap back, that may occur in the response of the structure. The method is a proven alternative for applications in masonry,⁵ reinforced concrete,⁶ and glass.⁷ Advancements in SLA include contributions to make the procedure mesh objective,^{4,6} saw-tooth laws for extremely brittle materials with snap back at constitutive level like glass,⁷ extension to non-proportional loading situations,⁸⁻¹² stepwise secant Coulomb friction laws,⁶ combined incremental-total approaches like non-iterative energy-based method and the automatic method,¹⁰ SLA in a stochastic setting,¹³ combining SLA with crack tracking technique,¹⁴ and mesh-free SLA.¹⁵ Despite the active contributions of several researchers, the topic of non-proportional loading in SLA continues to be a debated one. To this end, this article contributes to the extension of SLA to three-dimensional (3D) stress states, under non-proportional loading conditions, which, in turn, would enable structural level applications. Applications, thus far, have been restricted to two-dimensional (2D) and 3D continuum problems for proportional loading and solely 2D problems for non-proportional loading situations, in the total strain-based fixed smeared crack constitutive framework. For 3D stress states under non-proportional loading conditions, the lack of a closed-form solution for the critical load multiplier, with regard to damage initiation, was the hindrance to the identification of the critical integration point, which motivated this work, and accordingly, two solutions strategies are proposed to address the issue. Firstly, the workflow in SLA and the constitutive model for solid elements (3D stress state) are elaborated in Section 2. Then, the motivation for the 3D non-proportional loading strategy is briefed upon in Section 3. Subsequently, in Section 4, the two new methodologies enabling extension to 3D stress states in non-proportional loading are detailed upon, including a qualitative discussion corroborating the choice of the first method for further studies. Section 5 presents the 3D validation studies. This includes two academic cases of three-point bending tests of a beam (with and without prestress loads): one with a straight and the other with a skewed notch, and a more complex case of RC slabs subject to shear loads in combination with axial loads.¹⁶

2 | CONSTITUTIVE MODEL AND WORKFLOW

SLA is different from the traditional incremental-iterative approaches with regard to both the constitutive framework and the workflow. The details pertaining to these aspects of SLA are presented in this section.

2.1 | Constitutive relations

2.1.1 | Uniaxial saw-tooth laws

The core idea of the method is to discretize the uniaxial constitutive relation into a stepwise secant material law that can be looked at as an approximation. This is also referred to as the saw-tooth law owing to the way it is described. In principle, the material law is described as a series of successively reducing secant stiffnesses and strengths, starting from the initial elastic branch with the original Young's modulus of the material E_0 and the actual tensile strength (f_t). Whenever there is breach of the stress limit, the next secant relation with reduced strength and stiffness properties takes over from the previous secant branch. In this way, the tangential stiffness of the structure is not considered, which helps to avoid situations where the modulus would be negative or zero, potentially leading to ill conditioning of the finite element formulation. The process of reducing the stiffness upon attaining a stress limit is repeated until the stiffness of the structure has vanished, which corresponds to a state of complete damage. Upon being completely damaged (last saw tooth), the

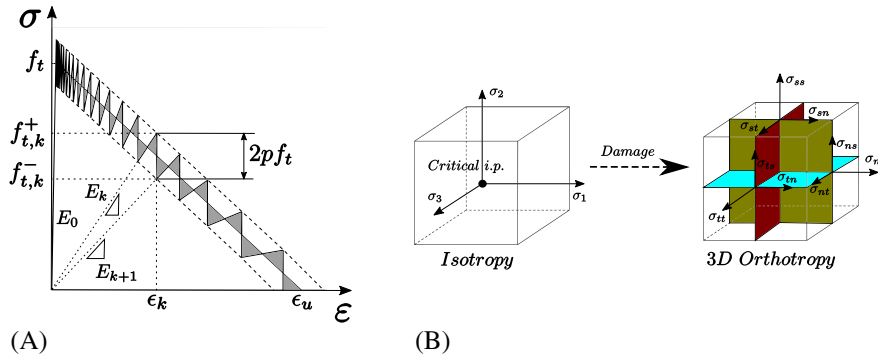


FIGURE 1 (A) Linear tension softening saw-tooth law based on the ripple-band approach and (B) the change in isotropic to orthotropic formulation upon damage initiation

element can either be removed while using an isotropic law for all directions or be provided a small dummy stiffness in an orthotropic fixed smeared crack setup for computational ease. This concept can be applied to various existing uniaxial laws like the linear tensile softening, exponential tension softening, and parabolic compressive softening to name a few.

Initially, the saw-tooth laws were generated by consecutively reducing Young's modulus and/or strength. However, these proved to generate mesh objectivity problems with respect to capacity and energy dissipation, and consequently, a simple regularization procedure was applied wherein the strength or the ultimate strain or even both are updated to keep the energy invariant, with the latter being reported as the most effective.³ Eventually, moving towards a more general approach to achieve mesh objective results, a ripple bandwidth concept was introduced,⁴ wherein a strength range is defined as a percentage of the maximum strength of the base curve. A band was introduced into the softening part enclosing the base curve such that the upper and lower triangles cancel each other out and eventually yield the same fracture energy (see Figure 1). More recently, an improved ripple bandwidth approach was presented pointing out that the vertical shifts of the base material law that define the original ripple band approach need not necessarily be equal.⁶ However, in this study, linear tension softening and parabolic compressive softening relations with the original ripple band approach are used, unless specified otherwise.

2.1.2 | Orthotropic 3D fixed smeared crack model

SLA for continuum problems is based on a total strain-based smeared cracking model with the fixed crack approach. There have been rotating crack models in the context of SLA¹⁷ with simplifications wherein the load multiplier is calculated with respect to the last equilibrated direction of a damaged integration point. This is done because the rotation of the principal strain is not known a priori but is an assumption that stands true only if no rotation occurs. Furthermore, other damaged integration points that should undergo rotation of the crack system to avoid shear stresses are not allowed to, since this would necessitate an iterative process to arrive at equilibrium.

In this study, the fixed crack model extended to 3D stress states is elaborated upon. As soon as the principal stress violates the allowable strength at an integration point, the isotropic stress-strain relation $\sigma = \mathbf{D}\epsilon$ transforms into a 3D orthotropic relation as $\sigma_{nst} = \mathbf{D}_{nst}\epsilon_{nst}$ and the *nst* cracked coordinate system is fixed along the directions of the principal stresses. In the primary principal stress direction, the Young's modulus and strength are reduced according to the uniaxial saw-tooth law. Subsequently, in the event of principal stress rotations, redistribution of stresses or application of another load non-proportionally, the stresses in the tangential directions of the aforementioned fixed crack system (secondary or tertiary) may violate the allowable strength and damage is introduced accordingly in the corresponding directions. Thus, every integration point essentially requires three uniaxial saw-tooth laws each for tension and compression in the 3D stress state. Besides, the shear behavior in the fixed cracking model is represented using a variable stepwise shear retention function that takes into account the reduction of shear stiffness with increasing damage in the normal direction of the cracked plane. Furthermore, the Poisson's ratio is reduced at the same rate as the associated Young's modulus. A simple Rankine-type biaxial failure surface is used to obtain combined tension-compression failures in the fixed crack setup. The 3D orthotropic compliance relation deduced from the isotropic relation $\epsilon = \mathbf{C}\sigma$, using the individual uniaxial

stress-strain relations—based on Hooke's law in Voigt notation, is given by

$$\begin{bmatrix} \varepsilon_{xx} \\ \varepsilon_{yy} \\ \varepsilon_{zz} \\ \gamma_{xy} \\ \gamma_{yz} \\ \gamma_{zx} \end{bmatrix} = \begin{bmatrix} \frac{1}{E_x} & \frac{-\nu_{xy}}{E_y} & \frac{-\nu_{xz}}{E_z} & 0 & 0 & 0 \\ \frac{-\nu_{yx}}{E_x} & \frac{1}{E_y} & \frac{-\nu_{yz}}{E_z} & 0 & 0 & 0 \\ \frac{-\nu_{zx}}{E_x} & \frac{-\nu_{zy}}{E_y} & \frac{1}{E_z} & 0 & 0 & 0 \\ 0 & 0 & 0 & \frac{1}{G_{xy}} & 0 & 0 \\ 0 & 0 & 0 & 0 & \frac{1}{G_{yz}} & 0 \\ 0 & 0 & 0 & 0 & 0 & \frac{1}{G_{zx}} \end{bmatrix} \begin{bmatrix} \sigma_{xx} \\ \sigma_{yy} \\ \sigma_{zz} \\ \sigma_{xy} \\ \sigma_{yz} \\ \sigma_{zx} \end{bmatrix}. \quad (2)$$

Due to the symmetry of the compliance matrix \mathbf{C} , the Poisson's ratios should be interrelated as well. Inverting the compliance matrix, we get the stiffness matrix \mathbf{D} as follows:

$$\mathbf{D} = A \begin{bmatrix} \left(\nu_{yz}^2 \frac{E_y}{E_z} - 1\right) E_x & -\left(\nu_{xy} + \nu_{yz} \nu_{zx} \frac{E_y}{E_x}\right) E_x & -\left(\nu_{xy} \nu_{yz} + \nu_{zx} \frac{E_z}{E_x}\right) E_x & 0 & 0 & 0 \\ -\left(\nu_{yz} \nu_{zx} + \nu_{xy} \frac{E_x}{E_y}\right) E_y & \left(\nu_{zx}^2 \frac{E_z}{E_x} - 1\right) E_y & -\left(\nu_{yz} + \nu_{xy} \nu_{zx} \frac{E_z}{E_y}\right) E_y & 0 & 0 & 0 \\ -\left(\nu_{zx} + \nu_{xy} \nu_{yz} \frac{E_x}{E_z}\right) E_z & -\left(\nu_{xy} \nu_{zx} + \nu_{yz} \frac{E_y}{E_z}\right) E_z & \left(\nu_{xy}^2 \frac{E_x}{E_y} - 1\right) E_z & 0 & 0 & 0 \\ 0 & 0 & 0 & \frac{G_{xy}}{A} & 0 & 0 \\ 0 & 0 & 0 & 0 & \frac{G_{yz}}{A} & 0 \\ 0 & 0 & 0 & 0 & 0 & \frac{G_{zx}}{A} \end{bmatrix}, \quad (3)$$

where

$$A = \frac{E_x E_y E_z}{-E_x E_y E_z + \nu_{xy}^2 E_x^2 E_z + \nu_{yz}^2 E_z^2 E_y + \nu_{zx}^2 E_y^2 E_x + 2\nu_{xy} \nu_{yz} \nu_{zx} E_x E_y E_z}. \quad (4)$$

For the initial uncracked stage, denoted by subscript 0,

$$E_x = E_y = E_z = E_0; \quad \nu_{xy} = \nu_{xz} = \nu_{yx} = \nu_{yz} = \nu_{zx} = \nu_{zy} = \nu_0; \quad G_{xy} = G_{yz} = G_{zx} = G_0 = \frac{E_0}{2(1 + \nu_0)}. \quad (5)$$

Upon crack initiation, the three axes of the orthotropic *nst* coordinate system are fixed. The *n*-axis is aligned with σ_1 and is perpendicular to the primary crack plane. The *st* plane covers the tangential crack directions, for which the directions are aligned with the principal stress directions σ_2 and σ_3 , respectively, at the onset of damage. When the failure type is compressive, the primary direction is that of the minimum principal stress. Consequently, the orthotropic relation becomes

$$\begin{bmatrix} \sigma_{nn} \\ \sigma_{ss} \\ \sigma_{tt} \\ \sigma_{ns} \\ \sigma_{st} \\ \sigma_{tn} \end{bmatrix} = \mathbf{D} \begin{bmatrix} \varepsilon_{nn} \\ \varepsilon_{ss} \\ \varepsilon_{tt} \\ \gamma_{ns} \\ \gamma_{st} \\ \gamma_{tn} \end{bmatrix}, \quad (6)$$

where the orthotropic stiffness matrix is similar to the aforementioned \mathbf{D} matrix with subscripts *n, s, t* instead of *x, y, z*.

In this formulation, Poisson effects and shear behavior can also be made damage based. That is, the shear stiffness is reduced in a stepwise fashion, directly dependent on the minimum of the corresponding Young's moduli, and likewise, the Poisson's ratios are reduced depending on their corresponding Young's modulus, as shown in the following. This variable shear retention approach is comparable to the ones adopted for plane stress⁶ and shell elements.¹⁸

$$\nu_{sn} = \nu_{tn} = \nu_0 \frac{E_n}{E_0} \quad \nu_{ns} = \nu_{ts} = \nu_0 \frac{E_s}{E_0} \quad \nu_{nt} = \nu_{st} = \nu_0 \frac{E_t}{E_0} \quad (7)$$

$$G_{ns} = \frac{\min(E_n, E_s)}{2 \left(1 + \nu_0 \frac{\min(E_n, E_s)}{E_0}\right)} \quad G_{st} = \frac{\min(E_s, E_t)}{2 \left(1 + \nu_0 \frac{\min(E_s, E_t)}{E_0}\right)} \quad G_{tn} = \frac{\min(E_t, E_n)}{2 \left(1 + \nu_0 \frac{\min(E_t, E_n)}{E_0}\right)} \quad (8)$$

Alternatively, Poisson's ratios could be set to zero at the onset of damage thereby decoupling the orthogonal behavior and the traditional constant shear retention could be used. Higher values of $\beta = 0.01$ or 0.1 , a constant shear retention factor, are generally used for standard NLFEA applications in concrete to simulate the aggregate interlock or lower values

to avoid stress locking problems. In this study, at onset of damage, $v_{ij} = 0$ and a constant shear retention factor $\beta = 0.0001$ are used, unless specified otherwise. Both choices could influence the crack propagation phase and the interaction of multiple cracks; however, considering the scope of this work to address the crack/damage initiation problem in a 3D stress state for non-proportional SLA (detailed further in Section 3), the choices are deemed reasonable.

Furthermore, in the current framework, immediately upon violation of the allowable strengths either along the maximum or minimum principal stress direction, the transition from an isotropic to orthotropic formulation is made and the 3D orthogonal fixed crack system (nst) is established. Alternatively, the fixing of the secondary and tertiary directions of the crack system could be postponed until failure in secondary direction, due to violation of the allowable strength by the principal stress in that direction. This is a more realistic representation of the multidirectional cracking phenomenon in comparison to the simplified former approach but it is not investigated in the present contribution.

2.2 | Workflow

The procedure was initially developed for a proportional loading scheme, where the rate of change of all loads is the same. The extension of SLA to non-proportional loading, closer to real life loading situations, wherein problems arise with respect to finding the critical integration point and the load multiplier, was based on the principle of superposition of global stresses due to the non-proportional loads and, subsequently, using the principal stress theory to find a closed-form solution for the critical load multiplier.⁸ The simplest and most common case of non-proportional loading is when there are constant loads on the structure like dead loads, precompression, and overburden, and the structure is subsequently subject to variable loads like earthquake or wind loads. The aforementioned approach of DeJong et al⁸ was restricted to plane stress formulations where the closed-form solution was deducible from the principal stress theory and the resulting crack coordinate system was established for the secondary cracking to follow. Although redistribution is necessary to

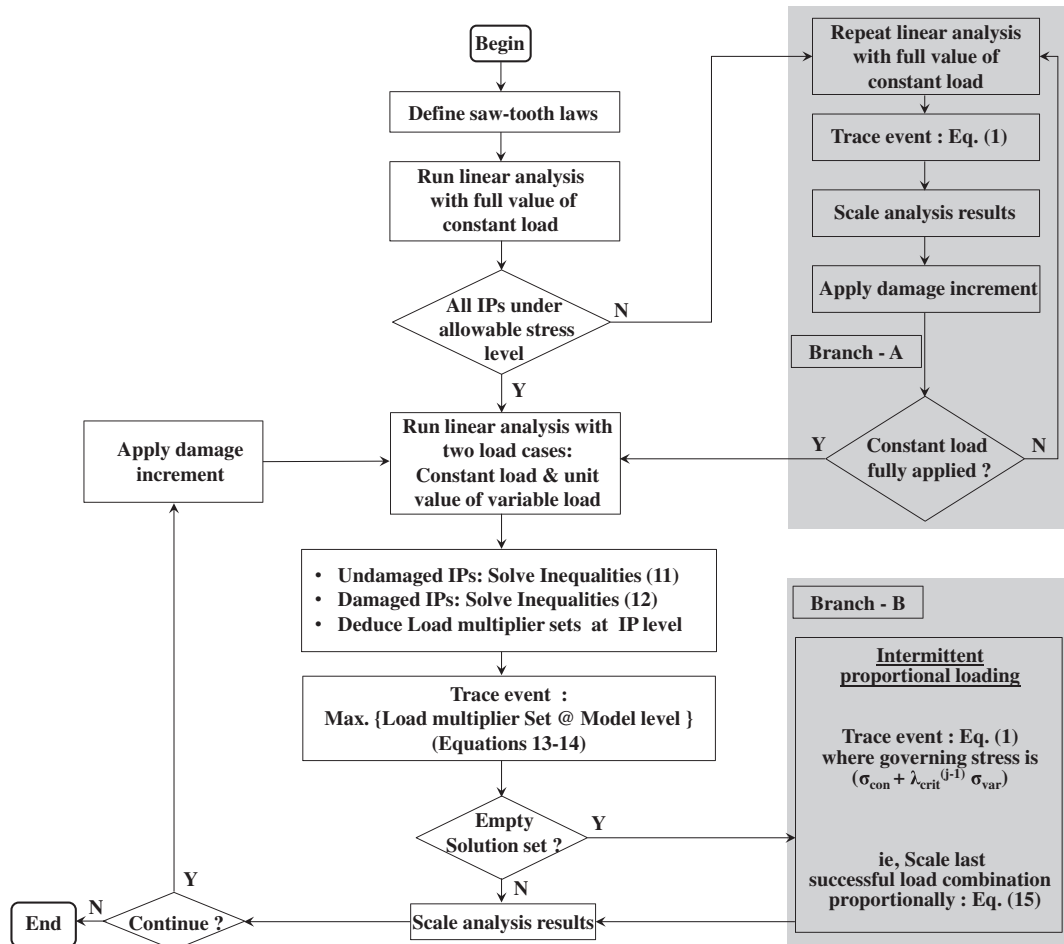


FIGURE 2 The general workflow in sequentially linear analysis for plane stress state with additional Branches: A for the case when damage occurs before the full application of constant loads, and B for addressing redistribution (IP refers to integration point)

simulate the dynamic phenomenon of cracking and crushing in a quasi-static setup of SLA, DeJong's approach overlooked this and allowed for temporary violation of constitutive laws when no admissible load multiplier could be found. This led to rupture under invalid stress fields and was pointed out by Eliáš et al.,⁹ wherein the force-release (F-R) method, an alternative to the non-proportional loading problem was presented. This work additionally aimed to address the dynamic phenomenon due to a damage event, which could lead to a series of subsequent failures in the vicinity of a damaged element, by redistributing the unbalanced forces gradually. It could be seen as a case of numerical damping in loading conditions or traditional dynamic relaxation that allows the system to pass through disequilibrium states before returning to a static equilibrium. Since it could not handle snap backs because of not being able to alter the previously applied load (constant load), the general method was proposed¹¹ of which the F-R and the load-unload methods (like SLA) are extreme cases, depending on time scales for the redistribution.

Simultaneously, a constrained maximization analogy with a double load multiplier strategy,⁶ one for constant and the other for variable loads ($F = \lambda_{\text{con}} F_{\text{con}} + \lambda_{\text{var}} F_{\text{var}}$, wherein $\lambda_{\text{con}} = 1$ and $\lambda_{\text{crit}} = \lambda_{\text{var}}$), was also conceived to address the redistribution phenomenon and was illustrated using continuum models for larger scale simulations like settlement of a building and pushover of masonry walls. The concept allowed for the redistribution of stresses, when no constitutively admissible* critical load multiplier could be found, by scaling the last successful scaled combination of constant and variable loads, which is referred to as the *intermittent proportional loading* hereon. Currently, the workflow of SLA is based on this approach and is detailed below for a 2D plane stress state (also see Figure 2).

1. Set up the saw-tooth laws as shown in Figure 1A.
2. Run a linear analysis with the full value of the constant load.
3. In case of damage already in this stage (nonlinearity):
 - (a) Identify the critical integration point with the least ratio of (f/σ_{gov}), where σ_{gov} is the governing principal stress and f is the allowable strength.
 - (b) Scale the constant load with the critical load multiplier (ie, the ratio from above).
 - (c) Reduce the strength and stiffness of the critical integration point based on the saw-tooth law.
 - (d) Return to step 2 and repeat until the scaled value of the constant load is the same as the original full value.
4. Once the constant load is fully applied, perform a linear analysis with the two load cases—one for the full constant load and the other for the variable load applied as a unit load.
5. Construct the global stresses as a superposition of the stresses due to the constant and variable loads (indicated with indices c and v , respectively) and express the resulting principal stress as a function of the load multiplier for the variable load (λ) as shown in the following:

$$\begin{aligned}\sigma_{xx} &= \sigma_{xx,c} + \lambda \sigma_{xx,v} \\ \sigma_{yy} &= \sigma_{yy,c} + \lambda \sigma_{yy,v}\end{aligned}\tag{9}$$

$$\begin{aligned}\sigma_{xy} &= \sigma_{xy,c} + \lambda \sigma_{xy,v} \\ \sigma_{1,2}(\lambda) &= \frac{1}{2}(\sigma_{xx} + \sigma_{yy}) \pm \sqrt{\frac{1}{4}(\sigma_{xx} - \sigma_{yy})^2 + (\sigma_{xy})^2}.\end{aligned}\tag{10}$$

6. Subsequently, two scenarios have to be considered.
 - (a) Damage initiation: For integration points that are *undamaged*, the principal stresses are limited to the tensile and compressive strengths (f_{ten} and f_{com}) resulting in quadratic inequalities in the load multiplier λ . Solving these as equations instead would yield a closed-form solution in λ for each governing principal stress. The resulting load multiplier would either be a maximum or minimum value corresponding to solving for the inequality $\sigma_{1,2}(\lambda) \leq f$ and eventually sets of values of λ per integration point i , Λ_i^{ten} and Λ_i^{com} , for tension and compression failures, respectively, are found.

$$\sigma_1(\lambda) \leq f_{\text{ten}} \text{ resulting in } \Lambda_i^{\text{ten}}\tag{11a}$$

$$\sigma_2(\lambda) \geq f_{\text{com}} \text{ resulting in } \Lambda_i^{\text{com}}\tag{11b}$$

*A constitutively admissible critical load multiplier refers to one that limits the stresses of each integration point in the FEM, including the critical one, to be less than or equal to the current strength of their respective saw-tooth laws, considering tension and compression criteria in all relevant directions.

- (b) Damage propagation: For integration points that are already *damaged*, the fixed crack system nt is already known. Therefore, for such points, the scaled combination of constant and variable loads in each of the orthogonal failure directions n and t is limited to the current allowable strength on the saw-tooth, resulting in linear inequalities. Again, solving for these inequalities results in sets of values of λ per integration point per failure direction. For simplicity, only the tensile failure relations are shown in the following.

$$\sigma_{nn,c} + \lambda_{nn}\sigma_{nn,v} \leq f_{ten,nn} \quad (12a)$$

$$\sigma_{tt,c} + \lambda_{tt}\sigma_{tt,v} \leq f_{ten,tt} \quad (12b)$$

7. The sets of constitutively admissible range of λ values from the damaged and undamaged integration points are subsequently assembled to find a common subset that would reflect the set of constitutively admissible range of load multipliers at the model level for the current analysis j . This would yield two scenarios as listed in the following.

- (a) Non-Zero solution set: The maximum of the common subset is denoted as the critical load multiplier λ_{crit} for N number of events.

$$\Lambda_{model}^j = \bigcap_{i=1}^N \Lambda_i^j \quad (13a)$$

$$\lambda_{crit}^j = \max(\Lambda_{model}^j) \quad (13b)$$

$$F_{crit}^j = \lambda_{con}F_{con} + \lambda_{var}F_{var}, \text{ where } \lambda_{con} = 1 \text{ and } \lambda_{var} = \lambda_{crit} \quad (14)$$

- (b) Empty solution set: When the stress states in two or more integration points do not allow for a common set of constitutively admissible scaled combination of the constant and variable loads, a return to an *intermittent proportional loading* is done. The *last successful load combination* is scaled in a proportional way thereby reducing the constant load temporarily and also partly retaining the scaled variable load.⁶ Determine the integration point for which the load multiplier λ is critical (least positive).

$$F_{crit}^j = \bar{\lambda}_{crit}^j (\lambda_{con}^{j-1} F_{con}^{j-1} + \lambda_{var}^{j-1} F_{var}^{j-1}), \text{ where } \bar{\lambda}_{crit}^j = \lambda_{crit}^j \quad (15)$$

8. Once the critical integration point and load multiplier are determined, scale the stresses and strains accordingly and obtain the new stress state.
9. Remove all loads and update the strength and stiffness of the critical integration point based on the saw-tooth law and return to step 4 until the element/structure is completely damaged.

3 | MOTIVATION FOR 3D NON-PROPORTIONAL LOADING STRATEGY

Structural level applications of SLA, for instance, a pushover analysis of a masonry or reinforced concrete building, would only be possible if the non-proportional loading strategy could be extended to 3D stress states. The principle of superposition of stresses due to non-proportional loads and the total strain-based fixed crack approach, with principal stress theory as failure criterion, has formed the basis of 2D continuum applications of SLA thus far. This approach relied on a closed-form solution for the critical load multiplier (for damage initiation) which, in turn, depended on the existence of a rather simple expression for the principal stress like the one in Equation (10) for the plane stress state. In an earlier attempt to extend SLA to 3D applications, DeJong et al¹⁸ made a simplification to at least enable use of shell elements. The formulation is similar to layered membrane elements spaced over the thickness of the shell, introduced through a 2D mesh with additional integration points in the thickness direction. These assumptions fix the crack plane to be perpendicular to the plane of the shell element and the shell mid-surface is aligned with the n -s coordinate plane. However, this membrane approach does not take into account the two out-of-plane shears in the calculation of the critical load multiplier. In conclusion, it was clear that deducing a similar expression for principal stresses from the characteristic cubic equation for a full 3D stress state was not as straightforward and thus had to be addressed. This has previously been touched upon motivating the need for an alternate non-proportional loading strategy called the sequentially linear

theta-based non-proportional strategy (SLTHNP),¹⁹ which is detailed upon in the next section. The characteristic equation in a 3D stress state is given by the equations as follows:

$$\det(\Sigma - \Lambda \mathbf{I}) = 0 \quad (16)$$

$$\begin{vmatrix} \sigma_{xx} - \Lambda & \sigma_{xy} & \sigma_{zx} \\ \sigma_{xy} & \sigma_{yy} - \Lambda & \sigma_{yz} \\ \sigma_{zx} & \sigma_{yz} & \sigma_{zz} - \Lambda \end{vmatrix} = 0 \quad (17)$$

$$\Lambda^3 - I_1 \Lambda^2 + I_2 \Lambda - I_3 = 0, \quad (18)$$

where Σ is the 3D stress tensor in matrix notation, Λ are the principal values- σ_1, σ_2 , and σ_3 , \mathbf{I} is the Identity matrix, and I_1, I_2 , and I_3 are the stress invariants. Mathematical procedures like Cardano's method²⁰ involving a transformation to get reduced cubic equations (a monic trinomial wherein the quadratic term is zero) and subsequent deduction of analytical solutions using trigonometric identities are well documented in literature. This forms the crux of the first method for 3D non-proportional SLA presented in the following section. Alternatively, a new non-proportional strategy suitable for the 3D stress states was introduced¹⁹ wherein the non-proportional loading problem statement was reformulated as a 2D optimization case, with respect to the directional cosines, and this is the second approach described in the next section.

4 | METHODOLOGIES

4.1 | Problem statement

The bottleneck for non-proportional loading applications in SLA for 3D stress states, as explained above, is the determination of load multiplier for damage initiation. Analogous to Equations (11), cubic inequalities have to be solved for both tension and compression failure per undamaged integration point and immediately establish the 3D orthogonal fixed crack system *nst* along the directions of the principal stresses at the onset of damage.

$$\sigma_1(\lambda) \leq f_{\text{ten}} \text{ resulting in } \Lambda_i^{\text{ten}} \quad (19a)$$

$$\sigma_3(\lambda) \geq f_{\text{com}} \text{ resulting in } \Lambda_i^{\text{com}} \quad (19b)$$

In the case of damaged integration points, analogous to Equations (12), linear inequalities have to be solved per direction of the *nst* crack coordinate system for both tensile and compressive failures, of which only the ones corresponding to tensile failure are shown below for the sake of simplicity. These, however, are rather straightforward to solve unlike Equations 19.

$$\sigma_{nn,c} + \lambda_{nn} \sigma_{nn,v} \leq f_{\text{ten},nn} \quad (20a)$$

$$\sigma_{ss,c} + \lambda_{ss} \sigma_{ss,v} \leq f_{\text{ten},ss} \quad (20b)$$

$$\sigma_{tt,c} + \lambda_{tt} \sigma_{tt,v} \leq f_{\text{ten},tt} \quad (20c)$$

Finally, the rest of the workflow is similar to that in the plane stress case, with respect to deducing the critical load multiplier as the maximum of the common subset of the set of constitutively admissible range of load multiplier values at the model level. Also analogously, in the event of an empty solution set, the procedure returns to the *intermittent proportional loading*.

4.2 | Analytical solution

This section elaborates on the analytical solution to find the critical load multiplier for 3D stress states, for undamaged integration points (see Equations (19)) in a fixed smeared crack setup. In line with the principle of superposition of stresses, first, the global stresses (shown in a general index notation in Equation (21)) are expressed as a scaled

combination of the non-proportional loads (constant loads depicted by subscript c and variable loads by subscript v) analogous to Equation (9).

$$\sigma_{ij} = \sigma_{ij,c} + \lambda \sigma_{ij,v} \quad (21)$$

$$I_1 = \sigma_{xx} + \sigma_{yy} + \sigma_{zz}$$

$$I_2 = \sigma_{xx}\sigma_{yy} + \sigma_{yy}\sigma_{zz} + \sigma_{zz}\sigma_{xx} - \sigma_{xy}^2 - \sigma_{yz}^2 - \sigma_{zx}^2 \quad (22)$$

$$I_3 = \sigma_{xx}\sigma_{yy}\sigma_{zz} + 2\sigma_{xy}\sigma_{yz}\sigma_{zx} - \sigma_{xx}\sigma_{yz}^2 - \sigma_{yy}\sigma_{zx}^2 - \sigma_{zz}\sigma_{xy}^2$$

$$f_{\text{ten}}^3 - I_1 f_{\text{ten}}^2 + I_2 f_{\text{ten}} - I_3 = 0 \quad (23a)$$

$$f_{\text{com}}^3 - I_1 f_{\text{com}}^2 + I_2 f_{\text{com}} - I_3 = 0 \quad (23b)$$

These global stresses in Equation (21) are subsequently substituted in the invariants I_1 , I_2 , and I_3 of the 3D stress tensor shown in Equation (22). Since we deal with combined tension-compression failures, principal stresses σ_1 and σ_3 will be relevant. Accordingly, we can obtain two separate cubic equations substituting the invariants of the stress tensor containing the superposed global stresses into Equation (18): one with $\Lambda = \sigma_1 = f_{\text{ten}}$ and another with $\Lambda = \sigma_3 = f_{\text{com}}$, where f_{ten} and f_{com} are the tensile and compressive strengths. The resulting cubic equations, shown in Equation 23 in a rather shortened sense, obtained by substitution of Equation (21) in Equation (22) and subsequently in Equation (18), are actually standard cubic equations in the load multiplier λ as shown in the following:

$$a\lambda^3 + b\lambda^2 + c\lambda + d = 0. \quad (24)$$

Without loss of generality, Equation (24) can be written as Equation (25) by manipulating the function to have coefficient $a = 1$ (dividing equation by a), whose coefficients \hat{b} , \hat{c} , and \hat{d} are detailed upon in the Appendix.

$$\lambda^3 + \hat{b}\lambda^2 + \hat{c}\lambda + \hat{d} = 0 \quad (25)$$

Subsequently, Equation (25) is transformed into a monic trinomial (or a depressed cubic equation) in a new variable α by substituting $\lambda = \alpha - \hat{b}/3$ as shown in the following:

$$\begin{aligned} \alpha^3 + P\alpha + Q &= 0, \\ \text{where } P &= \frac{3\hat{c} - \hat{b}^2}{3} \quad \& \quad Q = \frac{2\hat{b}^3 - 9\hat{b}\hat{c} + 27\hat{d}}{27}. \end{aligned} \quad (26)$$

The solution strategy is then chosen based on the discriminant D of Equation (26). If the discriminant shown in Equation (27) is less than or equal to zero, the depressed cubic equation would yield three real roots (of which at least two roots would be equal if $D = 0$), else if the discriminant is greater than zero, the cubic equation would yield only one real solution.

$$D = \left(\frac{P}{3}\right)^3 + \left(\frac{Q}{2}\right)^2 \quad (27)$$

In the former case, the three real solutions are obtained using trigonometric functions and the formulae²⁰ as shown in the following:

$$\alpha_k = 2\sqrt{-\frac{P}{3}} \cos\left(\frac{1}{3} \arccos\left(\frac{3Q}{2P}\sqrt{-\frac{3}{P}}\right) - \frac{2\pi k}{3}\right) \text{ for } k = 0, 1, 2. \quad (28)$$

In the latter case with the discriminant less than zero, the *Cardano* method²⁰ is used to find the real root. The complex roots are not of concern for our application; however, the physical meaning of the nature of the roots is discussed at the end of this section. This method involves introducing two new variables u and v linked by the condition $\alpha = u + v$ in the depressed cubic presented in Equation (26), followed by imposing a condition $3uv + P = 0$ and eventually solving a quadratic equation of which u^3 and v^3 are roots. For further details, please refer, eg, to the work of Birkhoff and MacLane.²⁰

$$u^3 = -\frac{Q}{2} + \sqrt{\frac{Q^2}{4} + \frac{P^3}{27}} \quad v^3 = -\frac{Q}{2} - \sqrt{\frac{Q^2}{4} + \frac{P^3}{27}} \quad (29)$$

$$\alpha_{\text{real}} = u + v$$

$$\alpha_{\text{complex1}} = -\frac{(u+v)}{2} + i(u-v)\frac{\sqrt{3}}{2} \quad (30)$$

$$\alpha_{\text{complex2}} = -\frac{(u+v)}{2} - i(u-v)\frac{\sqrt{3}}{2}$$

Once the real roots from the depressed cubic equation in α are determined, the actual load multipliers λ are determined using $\lambda = \alpha - \hat{b}/3$. The minimum positive value of the obtained real roots is subsequently tested on its possibility to be a maximum or a minimum load multiplier to satisfy the inequalities as in Equation 19, additionally subject to the condition that $\sigma_1 > \sigma_2 > \sigma_3$. This, in turn, will help deduce sets of the load multiplier λ values per undamaged integration point (Λ_i^{ten} or Λ_i^{com} as is the case), and thus, the critical load multiplier of an undamaged integration point is determined. Once an integration point is damaged, the crack coordinate system nst is set up. In subsequent SLA cycles for damaged integration points, three possible load multipliers are evaluated per analysis as shown in inequalities of Equation 20, corresponding to the three existing fixed failure directions (additionally for tension and compression damage possibilities per direction for triaxial failures), and eventually, the load multiplier sets per integration point are set up for both damaged and undamaged integration points. The critical load multiplier λ_{crit} for the system would be the maximum of the common subset of constitutively admissible load multipliers for both damaged and undamaged integration points or, in other words, the least positive of all maximum load multipliers from the individual sets. This is the constrained maximization approach as detailed in Section 2.2, which returns to the *intermittent proportional loading* in case of an empty solution set.

4.3 | SLTHNP: optimization problem

This section presents an alternative new approach for damage initiation in 3D non-proportional loading, wherein the problem is reformulated as a constrained optimization problem. For an undamaged integration point, the critical plane for crack/crush initiation is now identified by expressing the load multiplier λ as a function of the inclination of an arbitrary potential plane of damage, defined by θ for 2D plane stress states and by the two directional cosines l and m for 3D stress states, with respect to the reference coordinate system. The critical points of the function are deduced using optimization techniques and subsequently the critical load multiplier is established. This concept was first validated for 2D plane stress state to match up to the corresponding closed-form solution, elaborated in Section 2.2, in the work of Pari et al.¹⁹

Instead of resorting to the closed-form expressions of the eigenstresses from the principal stress theory to subsequently find the closed-form solution for λ , the normal stress on an arbitrary potential plane of damage is now expressed as a function of its inclination. In the 3D stress state, an arbitrary plane may be related to the reference coordinate system by means of the directional cosines l , m , and n , of which only two may be considered independent variables since they are related as $l^2 + m^2 + n^2 = 1$. The normal stresses acting on this plane due to the constant and variable loads (depicted by subscripts c and v , respectively) can thus be expressed in terms of the directional cosines and the load multiplier is now deduced as a function of two of these directional cosines, rewriting the third as $n = \sqrt{(1 - l^2 - m^2)}$:

$$\sigma_{nn,c} = \sigma_{xx,c}l^2 + \sigma_{yy,c}m^2 + \sigma_{zz,c}n^2 + 2\sigma_{xy,c}lm + 2\sigma_{yz,c}mn + 2\sigma_{xz,c}nl \quad (31)$$

$$\sigma_{nn,v} = \sigma_{xx,v}l^2 + \sigma_{yy,v}m^2 + \sigma_{zz,v}n^2 + 2\sigma_{xy,v}lm + 2\sigma_{yz,v}mn + 2\sigma_{xz,v}nl \quad (32)$$

$$\begin{aligned} \sigma_{nn,c}(l, m) + \lambda(l, m)\sigma_{nn,v}(l, m) &\leq f \\ \lambda(l, m) &= \frac{(f - \sigma_{nn,c}(l, m))}{\sigma_{nn,v}(l, m)} \quad \text{for } f = f_{\text{ten}} \text{ or } f_{\text{com}}. \end{aligned} \quad (33)$$

The idea is to find the values of λ , at which the slope of the function is zero, denoting the critical points of the function (namely, the maxima, the minima, and the saddle point), and the corresponding inclination of the plane defined by the directional cosines l, m, n is that of the plane of failure (cracking/crushing). This helps establish the 3D orthogonal smeared fixed crack directions (nst). The function of the load multiplier may be continuous or discontinuous for different stress states and typical functions of the load multiplier look like those shown in Figure 3. Firstly, the critical points of the functions are found per integration point, using optimization techniques, which are the bounds of the solution to the superposition of the non-proportional loads. These correspond to the limits of the sets of admissible values of λ per integration point as determined in Section 2.2 and the maximum λ of the common subset of all the integration points is chosen as the critical load multiplier for the system, similar to the 2D case. Additionally, analogous to the 2D case, for the new crack coordinate system at an inclination l, m , and n , with respect to the reference coordinate system, there will also be normal stresses σ_{tt} and σ_{ss} that are to be considered. That is, for the critical λ evaluated by finding the optimum l, m , and n , with respect to σ_{nn} , the corresponding σ_{tt} and σ_{ss} should be such that $\sigma_1 > \sigma_2 > \sigma_3$. This approach was referred to as the SLTHNP loading strategy and has been previously validated for plane stress state using benchmark studies.¹⁹

For the 2D plane stress state, the extrema (bounds) of the critical load multiplier were determined numerically using a one-dimensional (1D) optimization routine, since the load multiplier was a function of the inclination of the damage

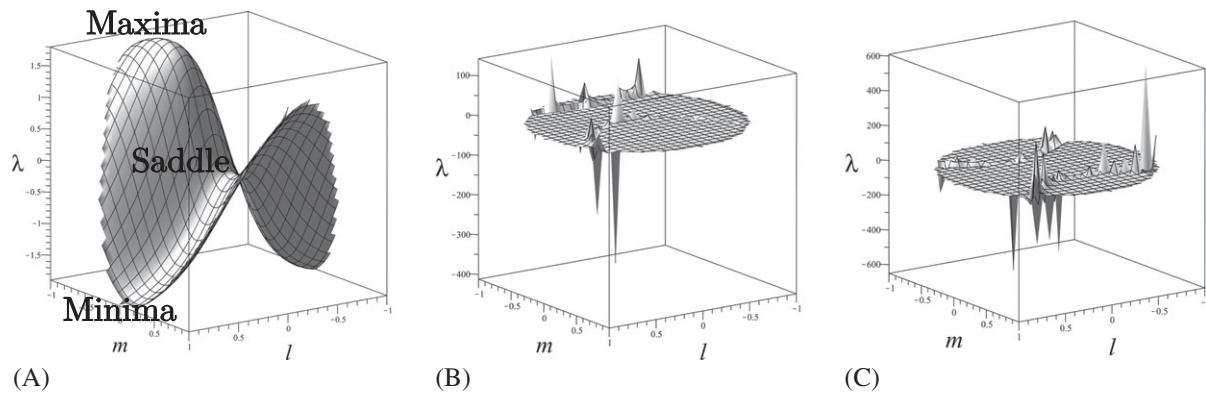


FIGURE 3 Typical continuous and discontinuous functions ((A), (B), and (C) corresponding to stress states I, II, and III mentioned in Table 1) of the load multiplier as a function of the directional cosines of a potential failure plane

TABLE 1 Stress components (in MPa) used for comparison of the two approaches

Stress State	Strength	σ_{xx}		σ_{yy}		σ_{zz}		σ_{xy}		σ_{yz}		σ_{zx}	
		$\sigma_{xx,c}$	$\sigma_{xx,v}$	$\sigma_{yy,c}$	$\sigma_{yy,v}$	$\sigma_{zz,c}$	$\sigma_{zz,v}$	$\sigma_{xy,c}$	$\sigma_{xy,v}$	$\sigma_{yz,c}$	$\sigma_{yz,v}$	$\sigma_{zx,c}$	$\sigma_{zx,v}$
I	0.25	4	2	-2.5	2	0.2	0.3	1	0.2	0.5	0.05	0.1	0.1
II	0.25	1	-2	0.5	2	0.2	0.3	1	0.2	0.5	1.25	0.1	0.1
III	0.25	4	2	2.5	-2	0.2	0.3	1	0.2	0.5	0.05	0.1	-0.1

plane, θ . It was easier to handle discontinuous functions at the 2D level because 1D (θ) optimization allows for bracketing of critical points, before using optimization techniques like the Brent's method (in combination with inverse quadratic interpolation) or the Golden search methods²¹ for subsequent isolation of the critical points. However, in the reformulated 3D non-proportional loading case, the optimization has to be done with respect to 2 variables l and m . Consequently, a multidimensional optimization routine is required and preliminary investigations were made with the rather basic downhill simplex method (Nelder-mead algorithm).²² The limitation, however, in multidimensional optimization is that the initial bracketing of the extremum or critical points is not possible anymore and emphasis has to be laid on possibly restarting the optimization routine from a “converged solution” repeatedly to ensure that the extremum is indeed the one sought for. The critical locations to be searched for in each function are points of zero slope, ie, the minima, maxima, and saddle point, which indicate the possible combinations of the load multiplier and potential failure planes. In a plane stress state, every stress state corresponded to two critical points in the range of $-\pi$ to π and the least positive value of all minima (points of negative second derivate) corresponded to the upper bound solution and the maximum positive value of all maxima (points of positive second derivate) corresponded to the lower bound. Along the same lines, we can formulate the bounds of the solution from the sets of three possible combinations per integration point in the 3D stress state and eventually arrive at the critical load multiplier for damage initiation. Once a point is damaged, the approach is similar to solving inequalities (20) and the rest of the workflow as mentioned in Section 4.1.

4.4 | Comparison of the approaches

In order to illustrate the two aforementioned approaches in Sections 4.2 and 4.3, three different stress states as shown in Table 1 are considered. The choice of these stress states is arbitrary and serves to only elucidate the possible combinations of the one/three real roots case from the analytical approach and the smooth/non-smooth functions from the optimization approach. The stress states as such have no significance. The analytical approach either yields one or three real roots depending on the discriminant of the depressed cubic function, Equation (26), in the load multiplier λ . If and only if $4P^3 + 27Q^2 \leq 0$, three real roots are obtained. When the discriminant $4P^3 + 27Q^2 > 0$, one would expect to have one real and two complex roots. However, only the real roots are of concern in determining the critical load multiplier as mentioned before. Although the complex roots for the scaling multiplier would result in one of the principal stresses (σ_1 or σ_3) being equal to the allowable strength, the other two principal stresses would result in complex values that are not representative of stress states in the case of classical continuum mechanics. Therefore, such roots are discarded.

TABLE 2 Solutions to the illustrative stress states

Stress State	Analytical Solutions			SLTHNP Optimization
	1st Root	2nd Root	3rd Root	
I	1.803	−0.061	−1.906	Continuous function (Figure 3A) with maxima, saddle and minima corresponding to three real roots
II	0.235	−0.092	−1.166	Discontinuous function (Figure 3B) with local critical points corresponding to three real roots
III	−1.89	$0.521 + 0.522i$	$0.521 - 0.522i$	Discontinuous function (Figure 3C) with one real root

Abbreviation: SLTHNP, sequentially linear *theta*-based non-proportional strategy.

The analytical solution to the three illustrative stress states are shown in Table 2. It has been observed in the validation studies that the case of three real roots dominate and there are very few instances of the “one real root” case.

With regard to the optimization approach for the three stress states considered, the corresponding load multiplier λ functions, with respect to the directional cosines l, m of the potential damage plane, are shown in Figure 3. The smooth function illustrated in Figure 3A, corresponding to stress state I in Table 1, could be representative of a local region in the discontinuous function displayed in Figures 3B and 3C. The critical points in the discontinuous functions shown in Figures 3B and 3C, corresponding to stress states II and III, are not visible owing to the large range of values in λ and also the rather non-smooth nature of the function. Accordingly, it is indeed difficult to deduce these points using optimization techniques. There seems to be no real correlation between the type/form of the discontinuous function and the nature of roots from the analytical approach vis-a-vis one or three real root cases. This is also reflected in the similarity of plots for the discontinuous functions in Figures 3B and 3C. Furthermore, the extreme peaks, that are not of concern for the current study, possibly refer to inclination of failure planes that are potentially not critical for the stress state caused by the scaled combination of the constant and variable loads. This is because we try to find bounds/limits for the solution, which are the least positive of all minima (the upper bound) and the maximum positive of all maxima (the lower bounds). Consequently, very large negative and positive values of the load multipliers are not of concern as they would be much farther from the solution bounds. With regard to the optimization approach, discontinuous functions, two typical ones as shown in Figures 3B and 3C, account for 99% of all stress states observed in the validation studies. However, since the success of such an approach relies heavily on the smoothness of the function, which is the case for most optimization methods, and non-smooth functions are often hard to handle, the SLTHNP approach could be cumbersome.

In conclusion, owing to the following reasons, the analytical approach is preferred over the optimization approach and all validation studies are consequently performed with the former.

- Discontinuous functions are hard to optimize for critical points because of the fact that
 - such methods may converge to points that are not necessarily the local critical points being sought for. This necessitates the need for multiple restarts to validate the converged solution or alternatively a very good first guess;
 - bracketing of critical points is not possible in multidimensional optimization methods like those in 1D methods like the Golden section search or Brent's methods,²¹

and consequently, the computational intensity of the optimization approach is higher than the analytical approach.

- Despite the computational effort, the solutions from the optimization approach may not be accurate enough, and therefore, the solution may trace through alternate equilibrium paths.

5 | VALIDATION STUDIES AGAINST EXPERIMENTAL BENCHMARKS

In order to verify the presented concept for 3D non-proportional loading, validation studies are carried out using 3D solid element finite element models (FEMs). A notched concrete beam tested in three-point bending with and without the effect of axial loads, a more complex case of a simply supported RC slab subjected to concentrated load near the supports with and without the effect of axial load, and, finally, a skewed notch concrete beam tested in three-point bending with additional prestress (to simulate 3D nonplanar curved cracks) are considered.

5.1 | Prestressed beams

Several three-point bending tests performed by Zhao et al.²³ were previously analyzed using SLA with plane stress assumptions.⁶ Of these beams, SG2-B1, of span 600 mm, 150 mm depth, and 120 mm thickness is chosen as reference for

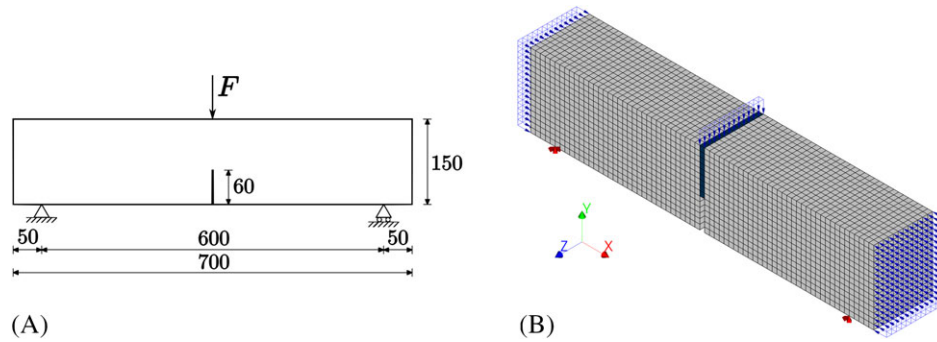


FIGURE 4 (A) Schematic representation of experiment Beam SG2-B1²³ and (B) finite element model of the same with axial loads [Colour figure can be viewed at wileyonlinelibrary.com]

this study but now in a 3D context. The beam is tested in three-point bending with a notch of 60 mm depth and 2 mm width, and a schematic representation of the experiment is shown in Figure 4. The load F results in a mid-span deflection u , which was measured at the load application point.

The middle of the beam is in pure bending (no shear), and therefore, the governing principal stress at the mid-section will align exactly with the longitudinal axis of the beam. If such a beam were to be subject to axial loads (purely for an investigation purpose) like a tensile or compressive prestress, the loading would become non-proportional. The effect of axial loads will either increase or decrease the capacity of a beam and has been a proven benchmark study for testing non-proportional loading strategy in SLA for the plane stress state thus far.⁸ Considering the simplicity of this case study and the fact that SLA introduces asymmetric failure propagation in FEM unlike traditional incremental iterative techniques (in this case with respect to an XY plane at the middle of the beam, See Figure 4, along its thickness), which, in turn, could yield stress situations that do not exactly resemble the aforementioned perfectly symmetric 2D stress situation, the SG2-B1 beam specimen subject to additional axial loads makes for a good case study to be investigated for validation purposes of the 3D non-proportional loading strategy, although it does not represent a truly 3D stress state that might result in 3D multidirectional cracking.

Finite element model

The simply supported beam is modeled with geometry as shown in Figure 4 except that the notch width is assumed to spread over an entire element length. The FEM is made using linear eight-noded isoparametric solid (brick) elements, with translational degrees of freedom and a reduced one-point Gaussian integration scheme. All elements are approximately 10 mm in size. Linear elements (ie, elements with linear interpolation shape functions) are used in order to ensure constant strain distribution over the entire element. This helps in symmetric assessment of the crack bandwidth that is then equal to the length of the element. Concrete has been modeled as a linear-elastic material everywhere except the notched column of elements, where all the physical nonlinearity is lumped. These elements along the notch are provided the possibility of tensile softening failure. The adopted saw-tooth law for these notched column of elements is of linear tension softening type, with material parameters mentioned in Table 3. Three cases are considered to address the

TABLE 3 Modeling and material parameters: prestressed beam

Parameters	Values
Young's Modulus E_o (GPa)	16
Poisson's ratio ν_o	0.15
Tensile strength f_t (MPa)	3.78
Mode I fracture energy G_f^I (N/mm)	0.224
Tension softening relation	Linear
Saw-tooth discretization factor (p)	0.15
No. of saw teeth	16
Compressive behavior	Linear elastic
Crack bandwidth h (mm)	10
Shear retention factor β	10^{-4}

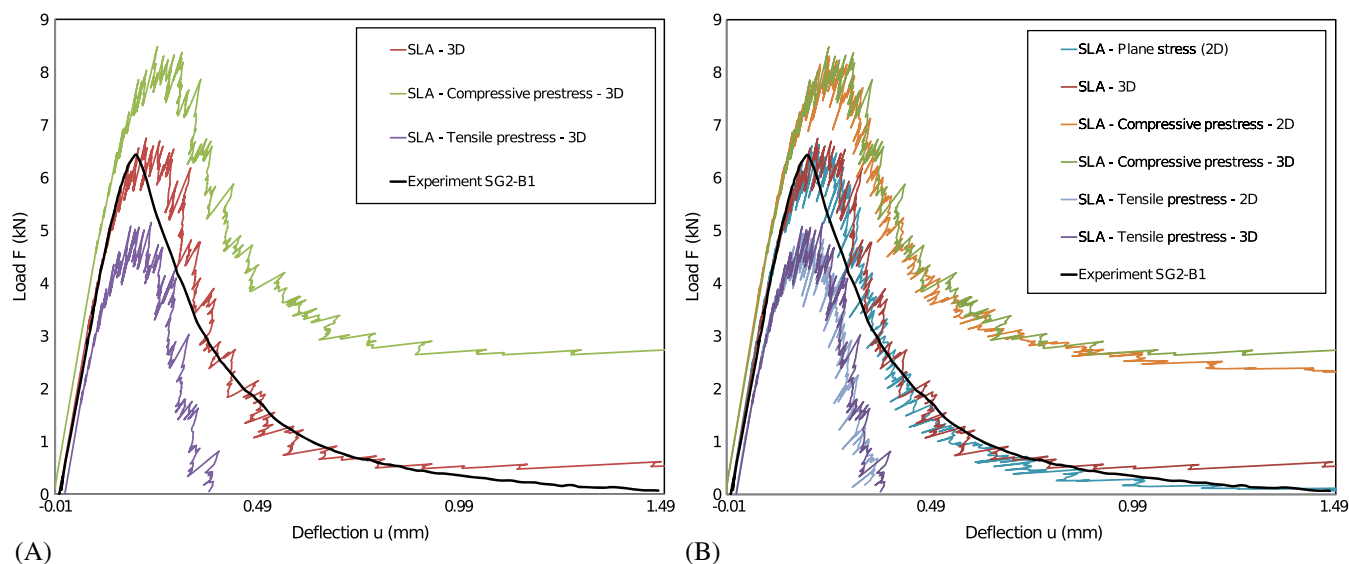


FIGURE 5 (A) Force displacement curves for the three-point bending cases using the three-dimensional (3D) model with and without axial loads and (B) its comparison against two-dimensional (2D) plane stress state simulations. SLA, sequentially linear analysis

non-proportional loading problem. First, the three-point bending test of SG2-B1 beam as in the experiment is simulated. Since the notch extends over one whole linear element, the point load is assumed to be equivalent to a distributed surface load applied at the top row of the central elements above the notch as shown in Figure 4. Second, the beam is additionally assumed to be subject to a uniform compressive prestress, of magnitude 0.25 MPa, at the ends of the beam. Finally, the beam is subject to a uniform tensile prestress, of magnitude 0.25 MPa, at the ends of the beam.

Results and discussion

To begin with, the force displacement curves from SLA, on the first case without axial loads, match up well with those from the experiment. Furthermore, the results from all three analyses show the propagation of the tensile crack through the height of the notch resulting in the reduction of effective cross-section of the beam. This behavior results in loss of flexural capacity and eventually is observed as the global softening in the force displacement curves shown in Figure 5. The qualitative behavior of all the three beams is similar barring the observed ultimate capacity. The presence of axial loads like the compressive prestress tends to delay the cracking and consequently results in a higher capacity. While on the contrary, due to tensile axial loads, the decrease in capacity is observed. The response from the three beams, therefore, qualitatively agrees to the expected response patterns from prestressed concrete theory. Additionally, it can also be observed that the force displacement curves match up to those obtained through 2D plane stress SLA simulations as shown in Figure 5B, thereby validating the 3D non-proportional strategy. With regard to the analytical solution of the load multiplier, obtained for undamaged integration points per analysis step, both the non-proportional cases of compressive and tensile axial loads yield three real roots always (not all were necessarily positive though). Additionally, the constant load, ie, the compressive or tensile axial load in both cases was kept constant throughout the analysis and there was no need to return to the *intermittent proportional loading*, which is *Branch-B* of the workflow in Figure 2. The use of a reduced one-point integration scheme gave symmetry with regard to the YZ plane through the mid-section but non-symmetry with respect to the XY plane, during the analysis steps, as only one integration point can become critical at a time and not two symmetric points (if present) of an element simultaneously. An interesting point of observation was that, while using a regular $2 \times 2 \times 2$ Gaussian integration scheme instead, the development of the crack through the thickness is rather stunted, while it is uniform in the plane stress state or the reduced integration study in the 3D model (Figure 6B). This is a case of alternating columns of elements, along the thickness of the beam, exhibiting crack localization (within the elements) and propagation in a zig-zag band of integration points (along either side of the notch) over the height of the beam, as shown in Figure 6C. This leaves some integration points of certain elements undamaged and therefore results in a lower peak capacity and lower dissipation of energy. The phenomenon is due to the inherent property of SLA in inducing asymmetry in localization rather than the fixed crack approach.

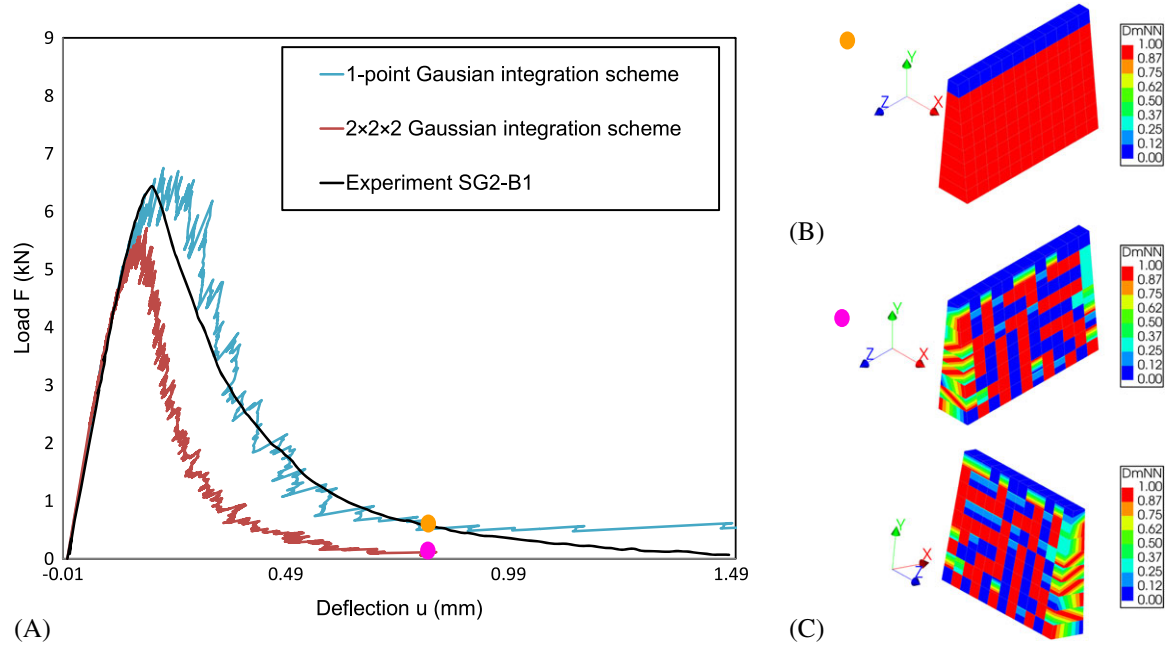


FIGURE 6 (A) Force displacement curves for the three-point bending beam (proportional loading) for different integration schemes and (B)-(C) their corresponding crack localization patterns

5.2 | RC slabs in shear failure

In order to corroborate the NP-strategy for full 3D cracking/failure possibilities, an RC slab tested in shear, along with axial loads to study the effect of prestressing, is chosen. A similar RC slab, also tested in shear, was simulated previously,⁶ although under proportional loading assumptions. The tests performed by Bui et al.,¹⁶ which are considered for this study, include a series of slabs tested in shear with either compressive or tensile axial loads, which would correspond to an increase or decrease in the shear strength of the RC slab, respectively. This is analogous to the prestressed beam cases presented in the previous section but will certainly result in more typical 3D cracking patterns. In this section, the experimental details are first described, with regard to the setup, crack patterns, and force displacement curves. Subsequently, the SLA simulations for the slabs are presented.

Experiments

An extensive experimental campaign was recently conducted¹⁶ to assess the shear strength of reinforced concrete slabs subject simultaneously to shear loads and axial tensile or compressive loads. The purpose of the study was to understand the effects of axial loading due to shrinkage, earthquakes, etc., on the shear resistance of RC slabs. To this end, eight simply supported (on all four sides) RC slabs of size $4\text{ m} \times 2.6\text{ m} \times 0.3\text{ m}$ were subject to concentrated loads near the supports.

All slabs were cast without shear reinforcement but were provided sufficient longitudinal and transverse reinforcements, to ensure the occurrence of shear failure over flexural failure. One reference slab (S2) was tested without axial forces while two slabs were tested with compressive axial loads of magnitude 1 MPa (SC1) and 1.5 MPa (SC2) and four slabs were tested with varying magnitudes of tensile axial loads ranging from 0.65 MPa to 1.2 MPa (ST1, ST2, ST3, and ST4). The axial loads were applied by means of 12 in-plane hydraulic jacks, while the concentrated load was applied using an out-of-plane hydraulic jack over a loading plate, at a distance of 560 mm from the nearest line support and 875 mm from the nearest edge. The experimental setup is shown in Figure 7. For further information about the experiments pertaining to the experimental setup, material properties, etc., the reader is referred to the work of Bui et al.¹⁶ Slabs S2 (without axial loads), SC2 (with 1.5 MPa compressive axial loads), and ST4 (with 1.2 MPa tensile axial loads) are chosen for this study. These would be analogous to the prestressed beam benchmark comparison and make for an ideal benchmark study to exemplify the newly introduced 3D non-proportional loading strategy.

All slabs were characterized by a similar failure mechanism, wherein firstly flexural cracks appeared at the bottom face along the transverse and longitudinal reinforcements followed by cracks due to a two-way shear slab mechanism (punching shear failure) with a perimeter crack surrounding the loaded area and, eventually, the pure shear failure occurred along the line support nearest to the loading plate (see Figure 8). The failure was quite brittle, more so in the case of slab

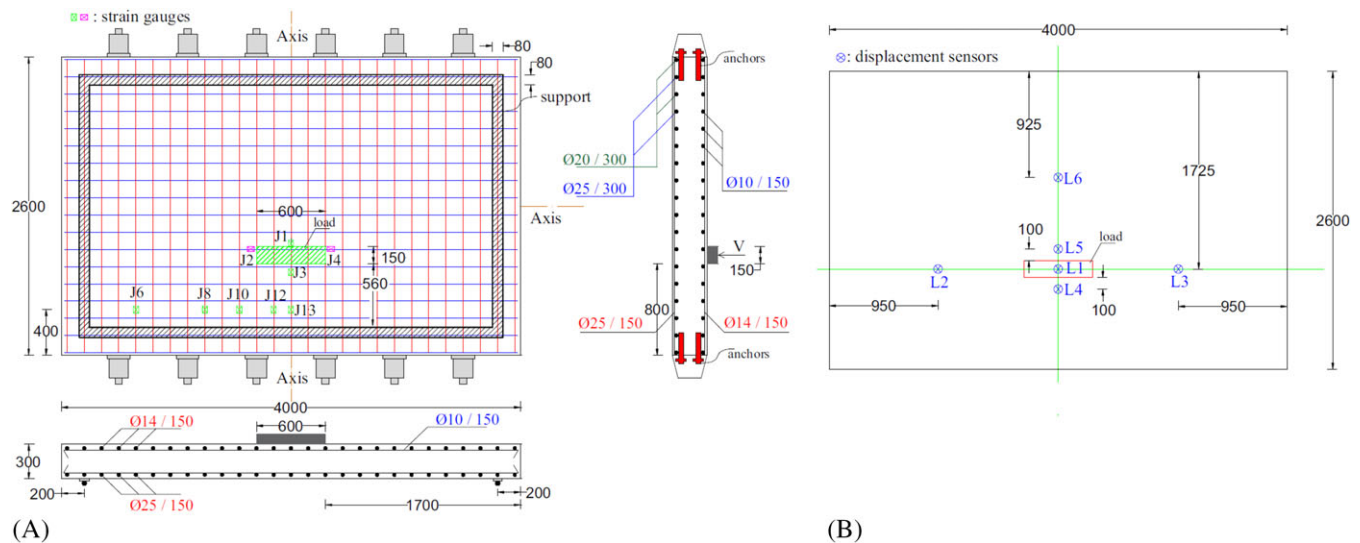


FIGURE 7 (A) Experimental setup: loading plate, reinforcements, axial load, and prestress application setup, and position of strain gauges J1-J13 to measure deformations in concrete along the reinforcements and (B) position of LVDT transducers L1-L6

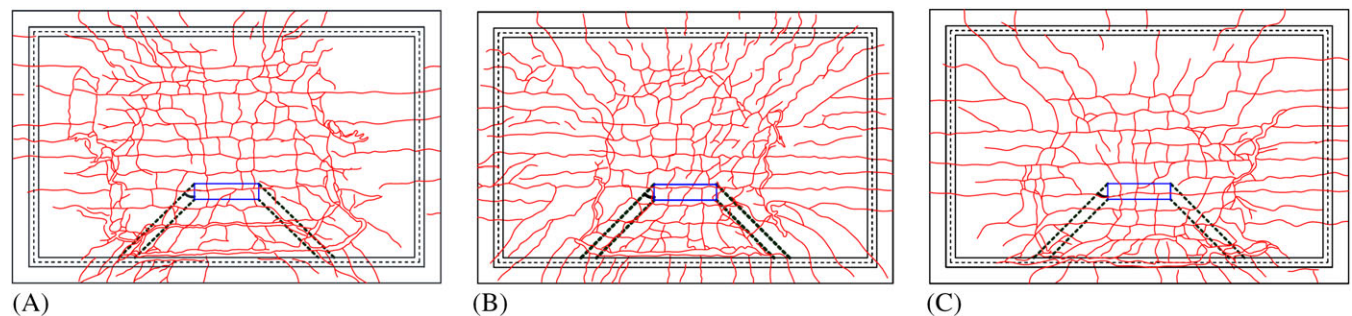


FIGURE 8 Experimental crack patterns of the bottom face of (A) slabs S2, (B) SC2, (C) and ST4. The black dashed lines from the loading plates to the supports denote the diagonal strut that determines the effective width for shear strength estimation¹⁶

SC2 with compressive prestress, and these aspects of the experiment also fit well with the possibility to observe post peak brittle failures with SLA. Figure 10A shows the force displacement relations of the applied load at the loading plate vs deflection at LVDT position L5 as shown in Figure 7B.

Finite element model

FEMs of the RC slab tests are made keeping in mind the constraints of SLA with regard to computational time. Consequently, only half the slabs are modeled because of the symmetry along the longitudinal direction. The loading plate and the support system of plates, to provide simple support all along the four sides, are both of uniform thickness of 20 mm and are provided linear elastic properties of steel. Both tensile and compressive softening possibilities (cracking and crushing) are provided to the concrete in the RC slab and the material properties for the same are mentioned in Table 4. The steel plates and the slabs are discretized by 20-noded quadratic isoparametric solid (brick) elements with translational degrees of freedom and a $3 \times 3 \times 3$ Gaussian integration scheme. Linear interface elements are provided between the steel plate and the slab to provide uniform contact between the slabs and the support/loading plate, as is done by the neoprene layer in the experimental setup. The number of elements in the direction of thickness (300 mm) is restricted to two and the size of most elements in the model is approximately between 100 and 150 mm. The reinforcements are modeled as an embedded system of bars and the constitutive behavior is kept linear elastic since the reinforcement ratios are quite high to result in flexural failure. This was also confirmed in a sensitivity analysis wherein the stresses in the reinforcements did not exceed 350 MPa. The FEM is as shown in Figure 9. Along the face of symmetry, the displacements along the X direction (longitudinal) are constrained (Figure 9A). The vertical support along Z axis is modeled using a single

TABLE 4 Modeling and material parameters: RC slabs

Material	Parameters	Slab S2	Slab SC-2	Slab ST-4
CONCRETE	Young's Modulus E_o (GPa)	15.875 ^a	15.375 ^a	16.2 ^a
	Poisson's ratio ν_o	0.15	0.15	0.15
	Tensile strength f_{tb} (MPa)	2.87	3.63	3.5
	Mode I fracture energy G_f^1 (N/mm)	0.175 ^b	0.177 ^b	0.178 ^b
	Tension softening relation	Linear	Linear	Linear
	Saw-tooth discretization factor (p)	0.15	0.15	0.15
	No. of saw teeth	9	9	9
	Compressive strength f_{cb} (N/mm ²)	30.91	33.3	30.91
	Compressive fracture energy G_c (N/mm)	43.75	44.25	43.75
	Compressive softening relation	Parabolic	Parabolic	Parabolic
	No. of saw teeth	12	12	12
REINFORCEMENTS & STEEL PLATES	Crack bandwidth h (mm)	Elem. size	Elem. size	Elem. size
	Shear retention factor β	10^{-4}	10^{-4}	10^{-4}
	Young's Modulus E_o [GPa]	210	210	210
	Poisson's ratio ν_o	0.3	0.3	0.3

^a50% of the reported Young's modulus in experiment to account for over stiff behavior.

^bValues deduced by preliminary calibration that are higher than the Mode-I fracture energy prescribed by MC2010.²⁴

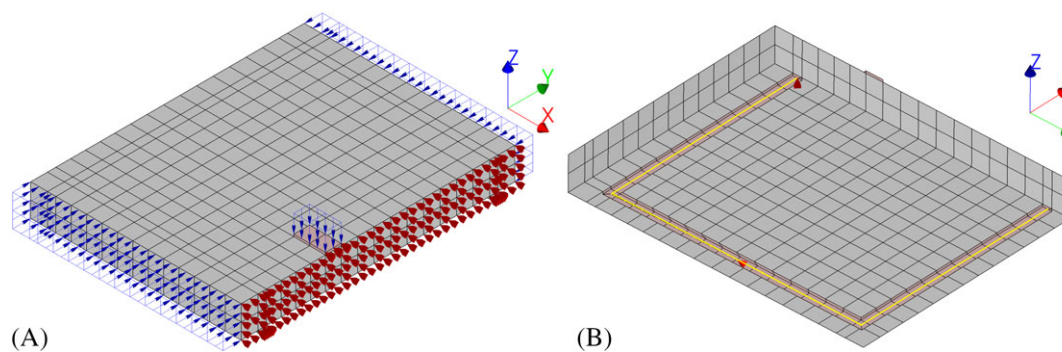


FIGURE 9 Finite element model of half of the RC slabs showing (A) the concentrated load on the loading plate, axial compressive loads, and constraints along the axis of symmetry and (B) the vertical support system

master node that is connected to the mid-line of the steel plate system (shown in yellow) using linear constraints as shown in Figure 9B. Also, a node right in the middle of the support plate in the transverse direction is supported along the Y direction to avoid the corresponding rigid body mode. The concentrated load on the loading plate near the support is applied as a unit distributed pressure load and axial loads of -1.5 MPa or 1.2 MPa are applied on either ends of the slab. The modeling parameters and material properties pertaining to each of the three analyses (reported by Bui et al¹⁶ unless stated otherwise) are summarized in Table 4.

Results and discussion

All three cases considered show initial cracking followed by a phase of reduction in stiffness wherein the two-way shear mechanism is observed to develop, before and around the peak load, culminating in the one-way brittle failure beyond the peak load. The numerical results qualitatively agree well with the experiments in terms of increase in load capacity with axial compressive loads and the contrary decrease in load capacity with axial tensile loads, see Figure 10B. The crack patterns shown in Figures 11, 12, and 13 are all in reasonable agreement to the experimental crack patterns in Figure 8 in terms of the development of the shear crack perimeter zone, formed due to the diagonal compression strut from the loading plate. Simultaneously, in the same figures, damage in the first failure direction of the *nst* orthogonal crack system expressed as $D = 1 - (E_{\text{current}}/E_{\text{original}})$ is also shown. $D_{\text{mNN}} = 0$ and 1 in these plots refer to undamaged and fully damaged cases in the *n* direction of an integration point. These plots correspond to the end of the brittle failures in the respective force displacement evolutions (yellow circular dots in Figures 14, 15, and 16).

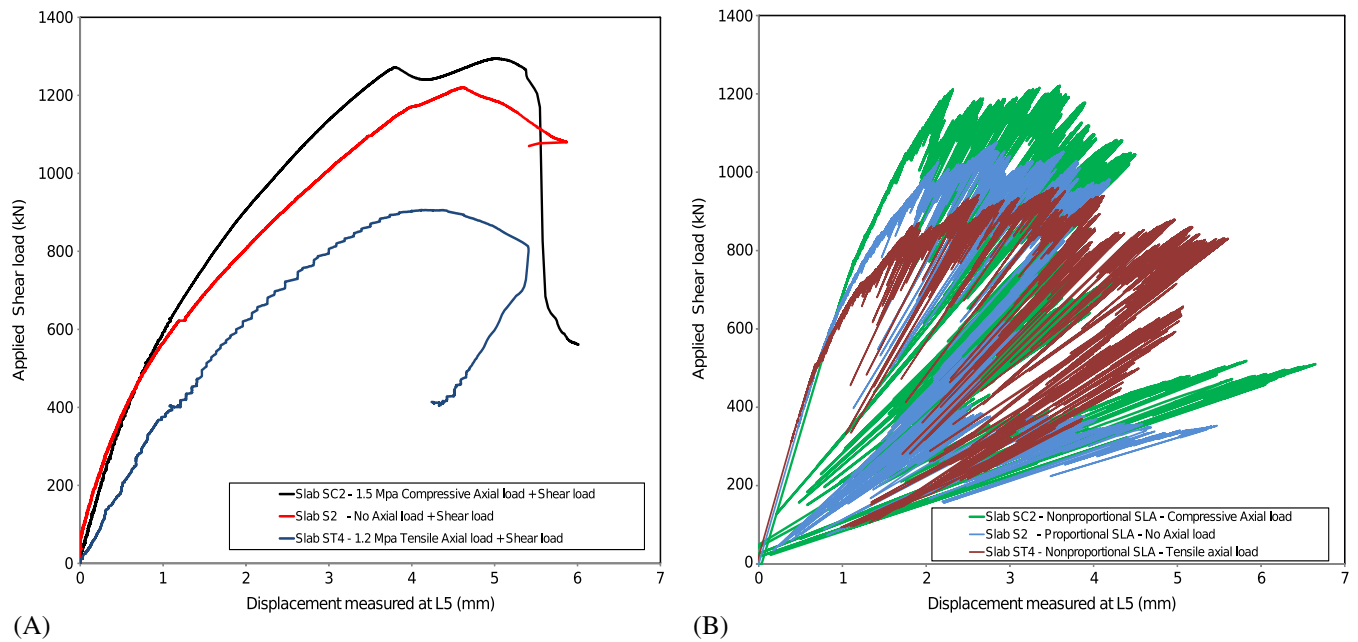


FIGURE 10 Force displacement curves for Slabs S2, SC2, and ST4 from (A) the Experiments and (B) monotonic sequentially linear analysis (SLA) simulations

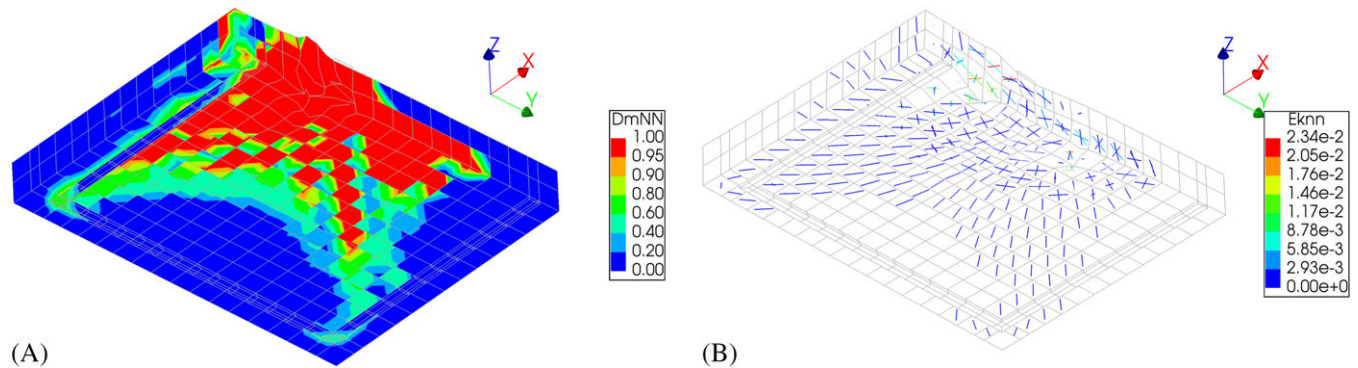


FIGURE 11 (A) Damage plots and (B) crack strain plots of half of slab S2's bottom face at the end of the brittle failure

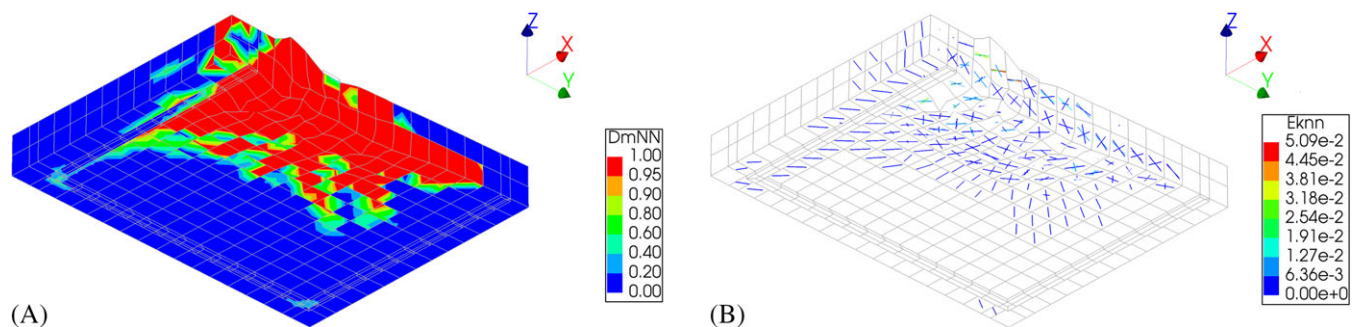


FIGURE 12 (A) Damage plots and (B) crack strain plots of half of slab SC2's bottom face at the end of the brittle failure

Furthermore, it has to be pointed out that the Young's moduli of all three specimen have been reduced to 50% of those reported in the experiments. With the original values of stiffness, an overly stiff behavior was observed regardless of the slab. This is also confirmed in the numerical simulations of the authors of the experimental campaign, using a concrete damage plasticity (CDP) model in combination with an explicit solver in the commercial finite element analysis (FEA)

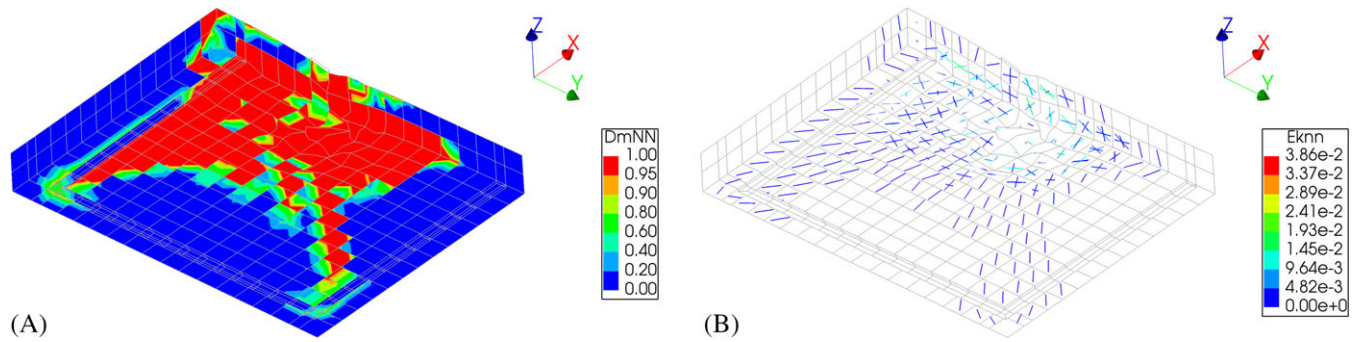


FIGURE 13 (A) Damage plots and (B) crack strain plots of half of slab ST4's bottom face at the end of the brittle failure

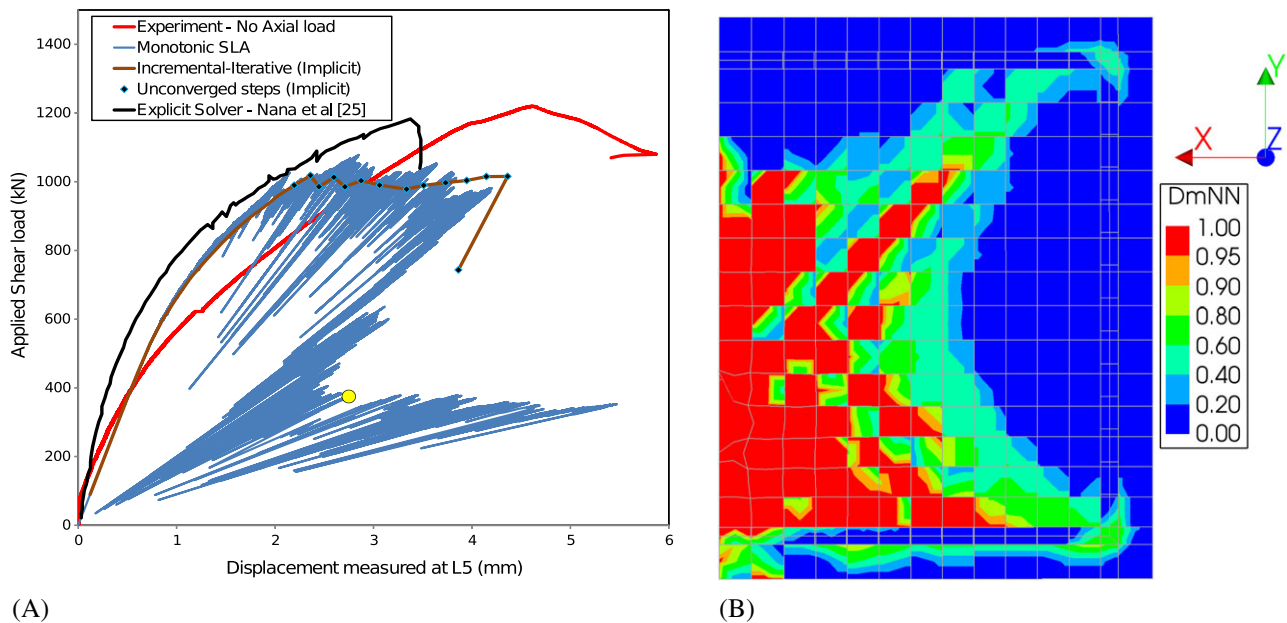


FIGURE 14 (A) Force displacement curves of the experiment vs proportional sequentially linear analysis (SLA) slab S2, additionally also showing the response using the traditional incremental-iterative procedure(implicit) and the explicit solver, and yellow circular dot denoting the reference point for end of brittle failure and (B) the damage plots from SLA of half of the slab at the reference point

program ABAQUS,²⁵ shown in Figure 14A. The flexible mortar bedding layer between the steel reaction support system and the slab was pointed out to be the source of this discrepancy. The FEM also has an interface between the steel frame and the slab, but this also does not help simulating the flexible behavior observed in the experiment. Accordingly, the decision to use reduced stiffness values was taken. However, despite reducing the stiffness, the force displacement relation of slab ST4 in particular seems to still be a lot stiffer than the experimental response. With regard to the experiments, the reduction in initial stiffness in the ST4 case, in comparison to slabs S2 and SC2, is in line with experimentally observed trend of decreasing initial elastic stiffness for increasing axial tensile loads (Slabs ST1-ST4),¹⁶ but this needs more clarity and insight. SLA simulations don't show such a decrease in stiffness, as seen in Figure 10B. Furthermore, the choice of two elements over the thickness was made keeping in mind the computational aspects of SLA as has been already mentioned. The mesh objectivity study is intended for future investigation after the completion of the development of a tailor-made linear solver for SLA, owing to very high computation times for finer meshes. Shear locking as expected, due to the lower shear retention factor used, is not a problem.

The results are presented individually, in terms of damage patterns at the end of the brittle failures in each of the three cases corresponding to the respective force displacement curves, in Figures 14, 15, and 16. Firstly, the proportional loading case of slab S2 is considered. The monotonic SLA simulation, with only the concentrated load, shows a clear brittle failure post peak. Although the material model allows for compressive failure, 3D orthogonal multidirectional cracking becomes decisive leading up to the brittle failure. This is very clear in the development of the diagonal tension cracking

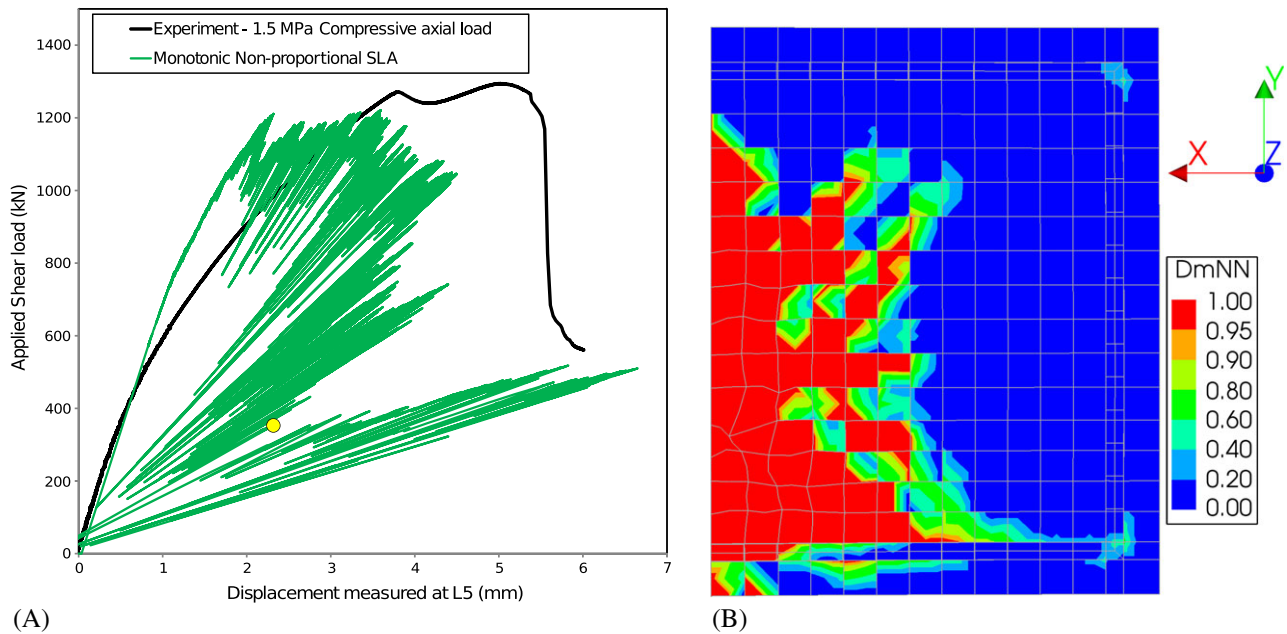


FIGURE 15 (A) Force displacement curves of the experiment vs non-proportional sequentially linear analysis (SLA) (Compressive prestress 1.5 MPa) slab SC2 and yellow circular dot denoting the reference point for end of brittle failure and (B) the damage plots from SLA of half of the slab at the reference point

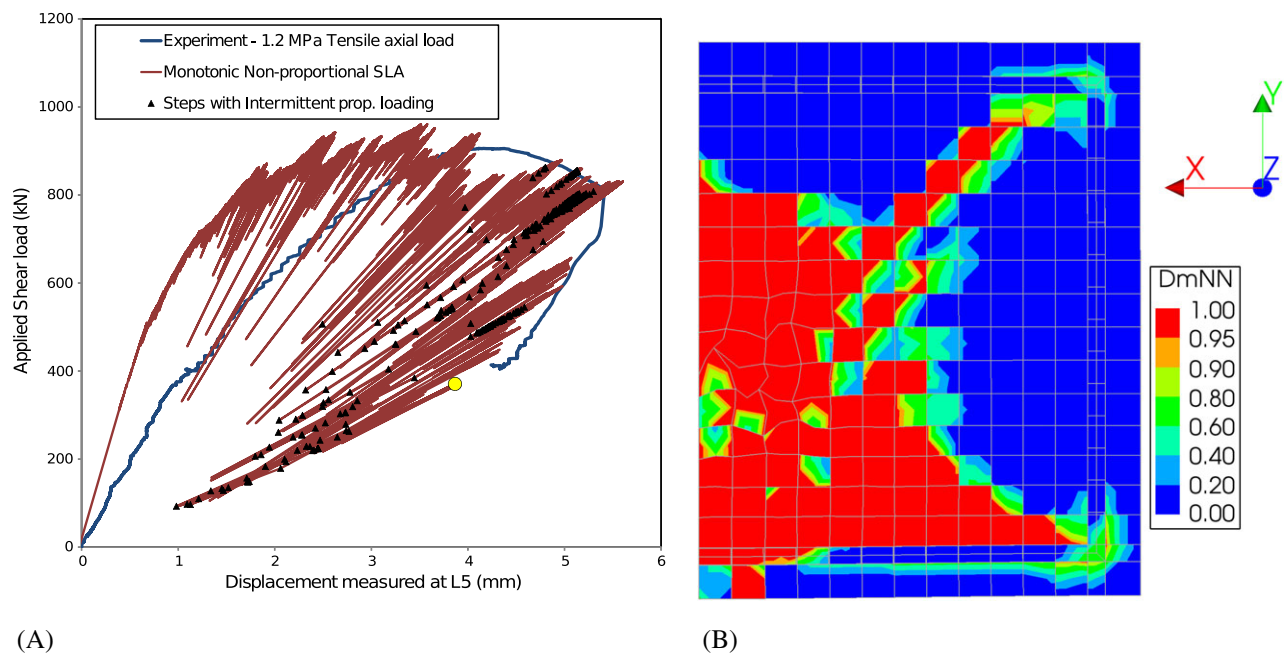


FIGURE 16 (A) Force displacement curves of the experiment vs non-proportional sequentially linear analysis (SLA) (tensile prestress: 1.2 MPa) slab ST4 and yellow circular dot denoting the reference point for end of brittle failure and (B) the damage plots from SLA of half of the slab at the reference point

from the loading area toward the support as shown in Figure 11B. Figure 14A additionally shows two other responses. One of the same FEM (material and modeling parameters as well) simulated using a traditional implicit solver (with a Newton-Raphson iteration scheme that would converge to an energy norm of 0.0001) in combination with an arc-length control in order to highlight the problems of non-convergence, and the other of a rather fine FEM with the CDP material model based explicit solver response.²⁵ Both do not give any insight into the post peak behavior that is rather well captured with the SLA procedure. Similar NLFEA for the non-proportional cases are not done owing to triviality.

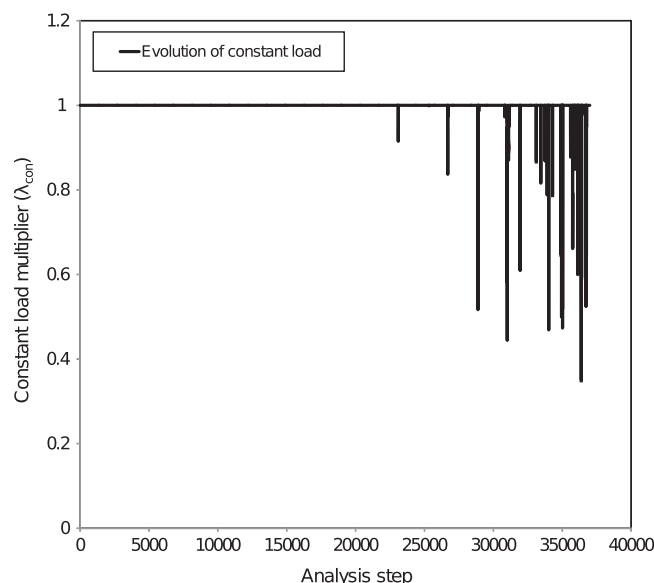


FIGURE 17 Evolution of constant load (tensile axial load) multiplier for the slab ST4 case

The aim of this study is to validate the 3D non-proportional loading in SLA and the results, in terms of delayed cracking in the compressive axial load case (SC2) and the reduced capacity in the tensile axial load case (ST4), exemplify the approach. Both the slabs SC2 and ST4 show the brittle collapse post peak due to the shear failure involving 3D orthogonal multidirectional cracking. The damage plots are shown alongside the force displacement evolutions in Figures 15 and 16 in relation to the point at the end of the brittle failure. Additionally, the corresponding crack strain plots are shown in an isometric view in Figures 12 and 13, which show the multidirectional cracking, the shear perimeter, and the highly deformed failing elements. Slab ST4 in particular is reported to have a much smaller shear crack perimeter than slabs S2, because of having a steeper diagonal strut due to the applied axial tension, but those from the simulations do not differ much. However, the reported relative increase in the ductility of the slabs in the case of axial tensile loads (ST1-ST4)¹⁶ is well captured in the SLA simulation of ST4.

With regard to the presented root finding algorithm for damage initiation in the 3D orthogonal fixed smeared cracking in the article, both slabs exhibit a small difference. Slab SC2, on the one hand, does not show any stress state all through the analysis involving complex roots. While slab ST4 involves a few analysis steps where one or two of the undamaged points' stress states yield complex roots. However, as explained in Section 4.4, these roots are not of significance and hence do not affect the non-proportional loading strategy. The slabs SC2 and ST4 also exhibit another difference with respect to the redistribution related to the double-load multiplier approach outlined in Section 2.2. On the one hand, the constant load is maintained at its fullest value all through the analysis in the case of slab SC2, implying no need for redistribution by returning to the *intermittent proportional loading*. Contrarily, slab ST4's SLA simulations involve the redistribution strategy towards the end of the analysis and this is exemplified in the evolution of the constant load multiplier as seen in Figure 17. However, there is no correlation between the observed “one real root” case and the onset of redistribution in any of the steps resulting in the *intermittent proportional loading*. The need for such a redistribution in a quasi-static setup of SLA for non-proportional SLA simulations is currently being investigated for cases when the constant load continues to drop gradually to very low values, indicating structural failure as has been previously interpreted¹⁹ and comparisons are being carried out between the available redistribution strategies^{9,12} in literature, in a smeared crack setup. Nevertheless, the constant load in this study of ST4 is restored to its full value after each set of these redistribution steps. Finally, although compressive nonlinearities are allowed in the material model, there were only few critical events involving compressive softening and therefore is not shown here since it is not decisive in the development of the mechanism.

5.3 | Nonplanar 3D curved crack evolution in plain concrete: prestressed beam case

The two validation studies presented thus far illustrate the capability of the methodology to capture 3D cracks in an SLA setup. The smeared distribution of damage, typically observed in reinforced concrete behavior, would camouflage the characteristic response of plain concrete fracture that is proven to be rather difficult to reproduce numerically.

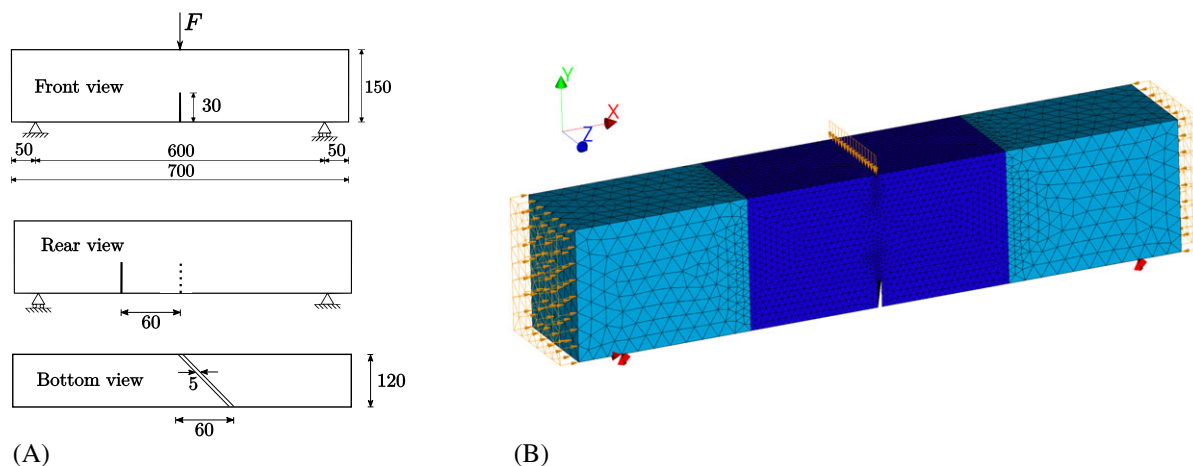


FIGURE 18 (A) Schematic representation of three-point bending test with a skew notch—30 mm deep and 5 mm wide and (B) finite element model of the same with axial loads

Therefore, modeling of 3D nonplanar curved cracks, in unreinforced concrete structures is addressed in this section. The 3D nonplanar crack propagation has been previously simulated by numerical techniques in literature^{26,27} but is mostly validated against experimental benchmarks like beams or cylindrical notched specimen loaded in torsion, three-point and four-point bending beams with eccentric/skewed notches, and wedge splitting tests to name a few, all of which are proportional loading cases. Owing to lack of experiments that are performed under non-proportional loading, an academic case study is considered in this section to illustrate the validity of the methodology. A three-point bending test, similar to the one presented in Section 5.1, is analyzed. The beam measures 600 mm, 150 mm, and 120 mm in span, depth, and thickness, respectively. However, contrary to the beam in Section 5.1, the depth of the notch is 30 mm, 5 mm wide, and is skewed. The inclination of the notch with longitudinal axis of the beam is $\tan(\theta) = 0.5$ and a schematic representation of the same is shown in Figure 18A. This beam is subjected to an additional compressive axial prestress, similar to the first case study. This non-proportional case is used to further validate the proposed methodology by comparing against an NLFEA response (using an implicit solver).

Finite element model

The FEM, shown in Figure 18B, is made using three-noded triangular isoparametric solid (brick) elements, with translational degrees of freedom and a reduced one-point Gaussian integration scheme. The choice of triangular elements was made to avoid mesh induced directional bias that would prove to be critical in achieving the curved nonplanar crack. Since the framework is that of smeared cracking, additional crack tracking algorithms¹⁴ could also help but this is outside the scope of the study. Concrete has been modeled as a linear-elastic material everywhere except the middle part of the beam, containing the inclined notch, which is shown in dark blue. All elements in this middle region are approximately 7.5 mm in size or lower and are provided the possibility of tensile softening failure. All other elements shown in light blue are approximately 20 mm in size. Linear elements (those with linear interpolation shape functions) are used in order to ensure constant strain distribution over the entire element. The adopted saw-tooth law for the middle part of the beam has the same linear tension softening material model and parameters as mentioned in Table 3, except for a couple of differences. The shear retention and Poisson effects are both made damage based as explained in Section 2.1.2 and the crack bandwidth relates to the size of the element. The point load is assumed to be equivalent to a distributed line load applied as shown in Figure 18B. The beam is additionally subject to a uniform compressive prestress, of magnitude 1.0 MPa, at the ends. Two SLA simulations are performed: one with only the bending load (proportional) and the other in combination with the prestress (non-proportional). The NLFEA simulations use the same parameters as their SLA counterparts except that the bending load is applied in displacement control, over 100 equal sized steps of magnitude 0.012 mm, with a Newton-Raphson iteration scheme that would converge to an energy norm of 0.0001.

Results and discussion

The results from SLA simulations of the both cases, with and without prestress, show the propagation of the 3D curved tensile crack through the height in a nonplanar fashion resulting in the reduction of effective cross-section of the beam. However, since the purpose of the study is to validate the non-proportional loading strategy, only the prestress case results

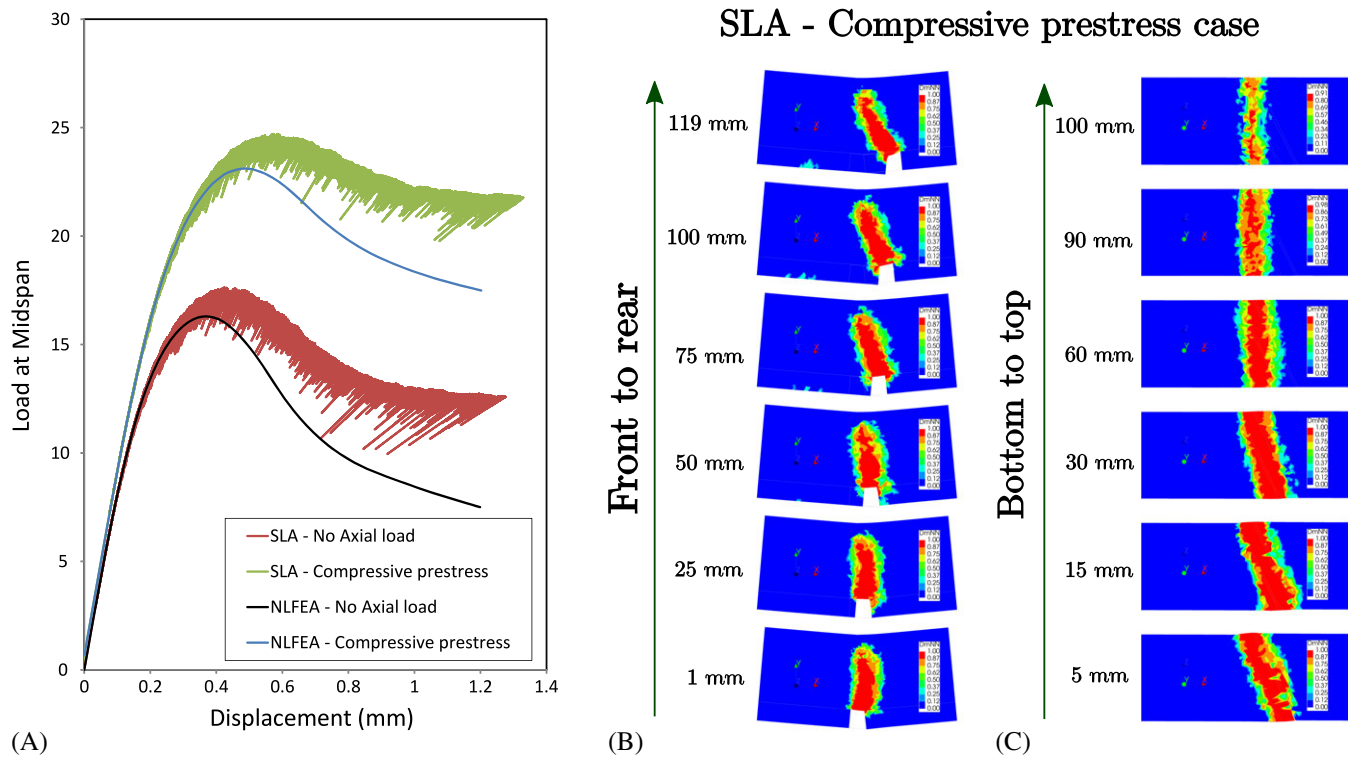


FIGURE 19 (A) Force displacement curves for sequentially linear analysis (SLA) and nonlinear finite element analysis (NLFEA) simulations; and damage plots for the prestress case using SLA shown as (B) front views along XY plane slices at several distances from front to rear of the beam (along Z: thickness of the beam) and (C) bottom views along XZ plane slices at several distances top of the notch to top of the beam (along Y: height of the beam)

from SLA are presented in Figures 19B and 19C. Herein, crack evolution is presented as damage plots for the middle portion of the beam (nonlinear material). In Figure 19B, the plots correspond to the front view along XY plane slices at several distances from front to rear of the beam (along Z axis: thickness of the beam). It is clear how the crack is straight at the front end and starts to incline towards the rear end, indicating nonplanarity about Z axis. In Figure 19C, the bottom view along XZ plane splices at several distances from top of the notch to the top of the beam are shown (along Y axis: height of the beam). It is evident that the crack is inclined at the bottom and starts to straighten towards the top of the beam, indicating nonplanarity about Y axis. YZ plane sections would not provide any new information and are therefore not shown. The results from NLFEA are in good agreement with those from SLA in terms of the twisted crack propagation and are therefore not shown.

The loss of cross-section due to the crack propagation results in loss of flexural capacity and eventually is observed as the global softening in the force displacement curves shown in Figure 19A. The presence of axial loads like the compressive prestress tends to delay the cracking and consequently results in a higher capacity, which is well captured and qualitatively agrees to the expected response patterns from prestressed concrete theory. Additionally, it can also be observed that both SLA responses (with and without axial loads) match up reasonably well to those obtained from NLFEA as shown in Figure 19A, thereby validating the 3D non-proportional strategy. The difference in the post peak behavior is due to the higher strength properties used because of the ripple band approach in SLA. With regard to the solution obtained for undamaged integration points per analysis step, the non-proportional loading case yields three real roots always (though not necessarily positive). Additionally, the constant load, ie, the compressive axial load, was kept constant throughout the analysis and there was no need to return to the *intermittent proportional loading*.

6 | CONCLUSIONS

This study contributes to extending SLA, a total approach to nonlinear FEA, to 3D applications with non-proportional loading. Two approaches have been presented to determine the load multiplier per undamaged integration point, in a 3D

stress state, for damage initiation under non-proportional loading. This, in turn, brings about a change from an isotropic to a 3D orthogonal fixed smeared crack formulation, with directions along those of the principal stresses at the onset of damage.

- The first approach involves deducing two cubic equations in the load multipliers (tension and compression failures), manipulating the equations into monic trinomials and subsequently solving these depressed cubic equations using the Cardano method or trigonometric solutions, for one or three real roots respectively, depending on the discriminant of the equation.
- The second approach involves a reformulation of the case as an optimization problem. The load multiplier is now expressed as a function of the inclination of a potential failure plane. The aim is to find solutions to the inclination of the critical plane, ie, the directional cosines and consequently determine the critical load multiplier. The second approach has previously been validated for 2D plane stress state. However, for 3D stress state, it is shown to be computationally intensive and also cannot guarantee solutions that match up to the analytical solution. The first approach is therefore preferred over the second for the validation studies, due to possibilities of loss of accuracy and computational efficiency reasons, but the validity of the concept as such remains.

The first concept is then validated against three case studies involving 3D stress states under non-proportional loading: a three-point bending beam (notched) test example with compressive and tensile prestress loads, an experimental campaign on the effect of axial loads on shear strength of RC slabs without shear reinforcement, and a three-point bending beam (skewed notch) example with a compressive prestress load. In the first case, the increase and decrease in capacity of the beam with compressive and tensile prestress, respectively, was well captured in the simulations. The second case of RC slabs also exhibited a similar trend in the shear strength capacity depending on the axial load applied and also showed a good-to-reasonable agreement in terms of damage patterns, force displacement curves, and the failure mechanism. The post peak brittle failure in all three cases was captured to good degree in SLA. In the third case, the increase in capacity of a bending beam (with a skewed notch) with additional compressive prestress was well captured in the SLA simulation along with a 3D nonplanar curved crack. With regard to the analytical solution presented in this article, all non-proportional loading cases of the prestressed beam studies and RC slabs, except the tensile axial load case of ST4, always resulted in three real roots and was rather easy to find in comparison to the SLTHNP optimization approach. Even in the case of slab ST4, 99% of all stress states in the analysis yielded three real roots analytically. The “one real root” case was sparsely observed but did not affect the non-proportional loading in any way. With regard to the redistribution strategy in returning to the *intermittent proportional loading*, all non-proportional case studies involved maintaining the constant load at its fullest value all through the analysis except in the ST4 slab case. However, even in that case, the redistribution was always followed by recovery of the full magnitude of the constant load. In conclusion, the case studies provide satisfactory results in terms of force displacement response and damage patterns, thereby proving the validity of the 3D non-proportional loading strategy for SLA.

In addition to the work presented in this article, several avenues in SLA are currently being investigated. To begin with, the computational performance of SLA, which has been highlighted as one of its major drawbacks, despite the robustness of the procedure, has been addressed using a new solver specifically designed for SLA by making use of the stiffness matrix from the previous solution. Moreover, to address issues pertaining to the fixed crack model, the constitutive modeling in SLA is now being extended to a rotating crack approach using the multilayer elastic brittle fraction approach.²⁸ Contributions in the aforementioned contexts are under different stages of progress and will ensue after the ongoing investigations.

ACKNOWLEDGEMENTS

This research was funded by Nederlandse Aardolie Maatschappij B.V. (NAM) under contract number UI46268 “Physical testing and modeling - masonry structures Groningen” as part of the NAM Hazard and Risk programme, which is gratefully acknowledged. The implementation of the presented concept was carried out in the commercial package DIANA and the authors are thankful for the collaboration with DIANA FEA B.V. towards the development of SLA and the forthcoming new implementations.

ORCID

Manimaran Pari  <https://orcid.org/0000-0002-9969-0843>

REFERENCES

- Gutiérrez MA. Energy release control for numerical simulations of failure in quasi-brittle solids. *Commun Numer Methods Eng*. 2004;20(1):19-29. <https://doi.org/10.1002/cnm.649>
- Rots JG. Sequentially linear continuum model for concrete fracture. *Fract Mech Concr Struct*. 2001;2:831-840.
- Rots JG, Invernizzi S. Regularized sequentially linear saw-tooth softening model. *Int J Numer Anal Methods Geomech*. 2004;28(7-8):821-856. <https://doi.org/10.1002/nag.371>
- Rots JG, Belletti B, Invernizzi S. Robust modeling of RC structures with an “event-by-event” strategy. *Eng Fract Mech*. 2008;75(3-4):590-614. <https://doi.org/10.1016/j.engfracmech.2007.03.027>
- Giardina G, van de Graaf AV, Hendriks MAN, Rots JG, Marini A. Numerical analysis of a masonry facade subject to tunnelling-induced settlements. *Engineering Structures*. 2013;54:234-247. <https://doi.org/10.1016/j.engstruct.2013.03.055>
- van de Graaf AV. *Sequentially Linear Analysis for Simulating Brittle Failure* [PhD thesis]. Delft, The Netherlands: Delft University of Technology; 2017.
- Invernizzi S, Trovato D, Hendriks M, van de Graaf AV. Sequentially linear modelling of local snap-back in extremely brittle structures. *Engineering Structures*. 2011;33(5):1617-1625. <https://doi.org/10.1016/j.engstruct.2011.01.031>
- DeJong MJ, Hendriks MAN, Rots JG. Sequentially linear analysis of fracture under non-proportional loading. *Eng Fract Mech*. 2008;75(18):5042-5056. <https://doi.org/10.1016/j.engfracmech.2008.07.003>
- Eliáš J, Frantík P, Vořechovsky M. Improved sequentially linear solution procedure. *Eng Fract Mech*. 2010;77(12):2263-2276. <https://doi.org/10.1016/j.engfracmech.2010.05.018>
- Graça-e-Costa R, Alfaiate J, Dias-da-Costa D, Neto P, Sluys LJ. Generalisation of non-iterative methods for the modelling of structures under non-proportional loading. *Int J Fract*. 2013;182(1):21-38. <https://doi.org/10.1007/s10704-013-9851-2>
- Eliáš J. Generalization of load-unload and force-release sequentially linear methods. *Int J Damage Mech*. 2015;24(2):279-293. <https://doi.org/10.1177/1056789514531001>
- Alfaiate J, Sluys LJ. On the use of non-iterative methods in cohesive fracture. *Int J Fract*. 2018;210(1-2):167-186. <https://doi.org/10.1007/s10704-018-0270-2>
- Georgioudakis M, Stefanou G, Papadrakakis M. Stochastic failure analysis of structures with softening materials. *Engineering Structures*. 2014;61:13-21. <https://doi.org/10.1016/j.engstruct.2014.01.002>
- Slobbe AT. *Propagation and Band Width of Smeared Cracks* [PhD thesis]. Delft, The Netherlands: Delft University of Technology; 2014.
- Salam Al-Sabah A, Laefer DF. Meshfree sequentially linear analysis of concrete. *J Comput Civ Eng*. 2015;30(2). Article No. 04015009. [https://doi.org/10.1061/\(ASCE\)CP.1943-5487.0000474](https://doi.org/10.1061/(ASCE)CP.1943-5487.0000474)
- Bui T, Nana W, Abouri S, Limam A, Tedoldi B, Roure T. Influence of uniaxial tension and compression on shear strength of concrete slabs without shear reinforcement under concentrated loads. *Construct Build Mater*. 2017;146:86-101. <https://doi.org/10.1016/j.conbuildmat.2017.04.068>
- Vorel J, Boshoff WP. Computational modelling of real structures made of strain-hardening cement-based composites. *Appl Math Comput*. 2015;267:562-570. <https://doi.org/10.1016/j.amc.2015.01.056>
- DeJong MJ, Belletti B, Hendriks MAN, Rots JG. Shell elements for sequentially linear analysis: lateral failure of masonry structures. *Engineering Structures*. 2009;31(7):1382-1392. <https://doi.org/10.1016/j.engstruct.2009.02.007>
- Pari M, Rots J, Hendriks M. Non-proportional loading for 3-d stress situations in sequentially linear analysis. In: Proceedings of the Conference on Computational Modelling of Concrete and Concrete Structures (EURO-C 2018); 2018; Bad Hofgastein, Austria.
- Birkhoff G, MacLane S. *A Survey of Modern Algebra*. Wellesley, MA: AK Peters, Ltd; 1997.
- Press WH, Teukolsky SA, Vetterling WT, Flannery BP. *Numerical Recipes: The Art of Scientific Computing*. 3rd ed. Cambridge, UK: Cambridge University Press; 2007.
- Press W, Teukolsky S, Vetterling W, Flannery B. Downhill Simplex Method in Multidimensions. *Numerical Recipes in C: The Art of Scientific Computing*. Cambridge, UK: Cambridge University Press; 1992.
- Zhao Z, Kwon SH, Shah SP. Effect of specimen size on fracture energy and softening curve of concrete: Part I. Experiments and fracture energy. *Cem Concr Res*. 2008;38(8-9):1049-1060. <https://doi.org/10.1016/j.cemconres.2008.03.017>
- Beverly P. *Fib Model Code for Concrete Structures 2010*. Hoboken, NJ: Ernst & Sohn; 2013.
- Nana WSA, Bui TT, Limam A, Abouri S. Experimental and numerical modelling of shear behaviour of full-scale RC slabs under concentrated loads. *Structures*. 2017;10:96-116. <https://doi.org/10.1016/J.ISTRUC.2017.02.004>
- Jäger P, Steinmann P, Kuhl E. Modeling three-dimensional crack propagation—a comparison of crack path tracking strategies. *Int J Numer Methods Eng*. 2008;76(9):1328-1352. <https://doi.org/10.1002/nme.2353>
- Ferté G, Massin P, Moës N. 3D crack propagation with cohesive elements in the extended finite element method. *Comput Methods Appl Mech Eng*. 2016. <https://doi.org/10.1016/j.cma.2015.11.018>
- Rots JG, Hendriks MA. Elastic-brittle fraction model for robust post-peak analysis of masonry structures. *Key Eng Mater*. 2014;624:27-39. <https://doi.org/10.4028/www.scientific.net/KEM.624.27>

How to cite this article: Pari M, Hendriks MAN, Rots JG. Non-proportional loading in sequentially linear analysis for 3D stress states. *Int J Numer Methods Eng*. 2019;119:506–531. <https://doi.org/10.1002/nme.6060>

APPENDIX

Characteristic equation in the 3D stress states given by Equation (18) transforms into the following equations by limiting the maximum (σ_1) and minimum principal stresses (σ_3) to the tensile (f_{ten}) and compressive strengths (f_{com}), respectively:

$$f_{\text{ten}}^3 - I_1 f_{\text{ten}}^2 + I_2 f_{\text{ten}} - I_3 = 0 \quad (\text{A1a})$$

$$f_{\text{com}}^3 - I_1 f_{\text{com}}^2 + I_2 f_{\text{com}} - I_3 = 0. \quad (\text{A1b})$$

The global stresses are expressed as a scaled combination of the non-proportional loads (constant loads depicted by subscript c and variable loads by subscript v), as in Equation (21) and subsequently substituted in the invariants I_1 , I_2 , and I_3 of the 3D stress tensor (Equation (22)) to give the following:

$$\sigma_{ij} = \sigma_{ij,c} + \lambda \sigma_{ij,v} \quad (\text{A2})$$

$$\begin{aligned} I_1 &= \sigma_{xx} + \sigma_{yy} + \sigma_{zz} \\ &= (\sigma_{xx,v} + \sigma_{yy,v} + \sigma_{zz,v}) \lambda + (\sigma_{xx,c} + \sigma_{yy,c} + \sigma_{zz,c}) \\ &= c_1 \lambda + d_1 \end{aligned} \quad (\text{A3})$$

$$\begin{aligned} I_2 &= \sigma_{xx}\sigma_{yy} + \sigma_{yy}\sigma_{zz} + \sigma_{zz}\sigma_{xx} - \sigma_{xy}^2 - \sigma_{yz}^2 - \sigma_{zx}^2 \\ &= (\sigma_{xx,v}\sigma_{yy,v} + \sigma_{xx,v}\sigma_{zz,v} - \sigma_{xy,v}^2 + \sigma_{yy,v}\sigma_{zz,v} - \sigma_{yz,v}^2 - \sigma_{zx,v}^2) \lambda^2 \\ &\quad + (\sigma_{xx,c}\sigma_{yy,v} + \sigma_{xx,c}\sigma_{zz,v} + \sigma_{xx,v}\sigma_{yy,c} + \sigma_{xx,v}\sigma_{zz,c} - 2\sigma_{xy,c}\sigma_{xy,v} + \sigma_{yy,c}\sigma_{zz,v} \\ &\quad + \sigma_{yy,v}\sigma_{zz,c} - 2\sigma_{yz,c}\sigma_{yz,v} - 2\sigma_{zx,c}\sigma_{zx,v}) \lambda \\ &\quad + (\sigma_{xx,c}\sigma_{yy,c} + \sigma_{xx,c}\sigma_{zz,c} - \sigma_{xy,c}^2 + \sigma_{yy,c}\sigma_{zz,c} - \sigma_{yz,c}^2 - \sigma_{zx,c}^2) \\ &= b_1 \lambda^2 + c_2 \lambda + d_1 \end{aligned} \quad (\text{A4})$$

$$\begin{aligned} I_3 &= \sigma_{xx}\sigma_{yy}\sigma_{zz} + 2\sigma_{xy}\sigma_{yz}\sigma_{zx} - \sigma_{xx}\sigma_{yz}^2 - \sigma_{yy}\sigma_{zx}^2 - \sigma_{zz}\sigma_{xy}^2 \\ &= (\sigma_{xx,v}\sigma_{yy,v}\sigma_{zz,v} - \sigma_{xx,v}\sigma_{yz,v}^2 - \sigma_{xy,v}^2\sigma_{zz,v} + 2\sigma_{xy,v}\sigma_{yz,v}\sigma_{zx,v} - \sigma_{yy,v}\sigma_{zx,v}^2) \lambda^3 \\ &\quad + ((\sigma_{xx,c}\sigma_{yy,v} + \sigma_{xx,v}\sigma_{yy,c})\sigma_{zz,v} + \sigma_{xx,v}\sigma_{yy,v}\sigma_{zz,c} - \sigma_{xx,c}\sigma_{yz,v}^2 - 2\sigma_{xx,v}\sigma_{yz,c}\sigma_{yz,v} \\ &\quad - 2\sigma_{xy,c}\sigma_{xy,v}\sigma_{zz,v} - \sigma_{xy,v}^2\sigma_{zz,c} + 2(\sigma_{xy,c}\sigma_{yz,v} + \sigma_{xy,v}\sigma_{yz,c})\sigma_{zx,v} + 2\sigma_{xy,v}\sigma_{yz,v}\sigma_{zx,c} \\ &\quad - \sigma_{yy,c}\sigma_{zx,v}^2 - 2\sigma_{yy,v}\sigma_{zx,c}\sigma_{zx,v}) \lambda^2 \\ &\quad + (\sigma_{xx,c}\sigma_{yy,c}\sigma_{zz,v} + (\sigma_{xx,c}\sigma_{yy,v} + \sigma_{xx,v}\sigma_{yy,c})\sigma_{zz,c} - 2\sigma_{xx,c}\sigma_{yz,c}\sigma_{yz,v} - \sigma_{xx,v}\sigma_{yz,c}^2 \\ &\quad - \sigma_{xy,c}^2\sigma_{zz,v} - 2\sigma_{xy,c}\sigma_{xy,v}\sigma_{zz,c} + 2\sigma_{xy,c}\sigma_{yz,c}\sigma_{zx,v} + 2(\sigma_{xy,c}\sigma_{yz,v} + \sigma_{xy,v}\sigma_{yz,c})\sigma_{zx,c} \\ &\quad - 2\sigma_{yy,c}\sigma_{zx,c}\sigma_{zx,v} - \sigma_{yy,v}\sigma_{zx,c}^2) \lambda \\ &\quad + (\sigma_{xx,c}\sigma_{yy,c}\sigma_{zz,c} - \sigma_{xx,c}\sigma_{yz,c}^2 - \sigma_{xy,c}^2\sigma_{zz,c} + 2\sigma_{xy,c}\sigma_{yz,c}\sigma_{zx,c} - \sigma_{yy,c}\sigma_{zx,c}^2) \\ &= a_1 \lambda^3 + b_2 \lambda^2 + c_3 \lambda + d_2. \end{aligned} \quad (\text{A5})$$

For demonstrative purposes, substituting the above equations in only the tensile part of Equations (A1a) yields

$$f_{\text{ten}}^3 - (c_1 \lambda + d_1) f_{\text{ten}}^2 + (b_1 \lambda^2 + c_2 \lambda + d_1) f_{\text{ten}} - (a_1 \lambda^3 + b_2 \lambda^2 + c_3 \lambda + d_2) = 0. \quad (\text{A6})$$

Rearranging the above equations in the form of Equation (24), we get

$$-a_1 \lambda^3 + (b_1 f_{\text{ten}} - b_2) \lambda^2 + (-c_1 f_{\text{ten}}^2 + c_2 f_{\text{ten}} - c_3) \lambda + (f_{\text{ten}}^3 - d_1 f_{\text{ten}}^2 + d_1 f_{\text{ten}} - d_2) = 0. \quad (\text{A7})$$

Dividing the above equation by $-a_1$, we get the depressed cubic equation

$$\lambda^3 - \frac{(b_1 f_{\text{ten}} - b_2)}{a_1} \lambda^2 - \frac{(-c_1 f_{\text{ten}}^2 + c_2 f_{\text{ten}} - c_3)}{a_1} \lambda - \frac{(f_{\text{ten}}^3 - d_1 f_{\text{ten}}^2 + d_1 f_{\text{ten}} - d_2)}{a_1} = 0, \quad (\text{A8})$$

which is similar to the form as in Equation (26) and the coefficients correspond to \hat{b} , \hat{c} and \hat{d} as in Equation (26), which is detailed upon further in analytical solution detailed in Section 4.2. These coefficients have to be written down hard-code to be able to subsequently solve the cubic equation, using either the Cardano method or the trigonometric solutions.